Plasmonic Laser Nanoablation of Solid Material

By

Daniel Steven Eversole, B.S.

Thesis

Presented to the Faculty of the Graduate School
of The University of Texas at Austin
in Partial Fulfillment
of the Requirements
for the Degree of

Master of Science

The University of Texas at Austin
December 2007

Plasmonic Laser Nanoablation of Solid Materials

APPROVED BY
SUPERVISING COMMITTEE:

Adela Ben-Yakar

Konstantin Sokolov

I dedicate this thesis to my family. Without all their love, encouragement, and support, I would not be where I am today.

Acknowledgements

There are many individuals that I wish to thank for their help over the years that has led to me being here at this point of my life. First and foremost, I would like to thank my advisor, Dr. Adela Ben-Yakar, who has been instrumental in making this project successful. Her trust in me has allowed me the opportunity to take the project from just an idea and develop it into a technique with a wide range of applications. Without our extensive and fruitful discussions and the generous funding to the project, the technique would not be as mature as it is today. Also, I would like to thank Dr. Frederic Bourgeois in all his help in times when the project just was not working or in spending late nights with me ablating samples. Additionally, I was able to formulate a lot of exciting ideas over our regular coffee house discussions. Thank you to Xun (Sam) Guo and Rick Harrison for their help with the setup and many sample ablations. Also, many thanks to Bill Lackowski and Yangming Sun for their assistance with the AFM and SEM, respectively. Also, I wish to express my gratitude to Dr. Kostia Sokolov for taking time out of his busy schedule to review this thesis and for being someone who was always available to answer questions when arisen. Finally, a special thanks to my family, friends, and past mentors, for their support throughout my education and providing the encouragement to fully realize my dreams. I especially wish to thank my grandfather for his constant support of my educational dreams.

December 2007

Plasmonic Laser Nanoablation of Solid Materials

Daniel Steven Eversole

The University of Texas at Austin, 2007

Supervisor: Adela Ben-Yakar

We experimentally demonstrate the fabrication of nanostructures ablated on silicon (100) and borosilicate glass substrates by the plasmonic scattering of 780 nm, 220 fs laser pulses in the near-field of gold nanospheres. We take advantage of the enhanced plasmonic scattering of ultrashort laser light in the particle near-field to ablate well-defined nanocraters. Gold nanospheres are deposited onto each substrate surface and irradiated with a single laser pulse. We studied the effect of laser polarization on the morphology of ablated nanostructures and estimated the minimum fluence for plasmonic nanoablation necessary for single particles and particle aggregates. Generated nanocrater morphologies show a direct imprint of the particle dipolar scattering region, as predicted in our theoretical calculations. The largest near-field enhancements for single particle ablation were found when the incident radiation was directed at a 45° angle into the substrate surface. Additionally, larger enhancements were measured for particle aggregates than single particles. The measured near-field enhancement values agree well with the maximum field enhancements obtained in our calculations. The agreement between theory and measurements supports that the nanocraters are indeed formed by the enhanced plasmonic scattering in the near-field of the nanoparticles.

Table of Contents

List of Figures

Chapter 1: Introduction

In recent years, there has been an extensive strive to develop novel laser ablation techniques for the nanomanufacturing of solid materials [1–15] as well as for the nanosurgery of biological structures with a submicron resolution [16–19]. Specifically, optical near-field technology has been presented as an attractive nanofabrication method because it spatially confines laser light to nanodomains below the diffraction limit to generate nanometer-scale features. Several near-field optical methods have been developed for nanolithography including, laser assisted scanning-tip patterning [1–4], near-field scanning optical microscope (SNOM) patterning [5–7], plasmonic lithography [8], contacting particle-lens array (CPLA) utilizing silica beads [9–11], and gold particles [12–15].

Submicron laser surgery techniques currently require the use of tightly focused ultrashort laser pulses to manipulate subcellular structures [16–19]. Limitations arise in the need for the target to be located with submicron resolution and systems are limited by diffraction. To achieve laser confinement below the diffraction limit in biological materials, we propose the use of gold nanoparticles. Noble metal nanoparticles exhibit strong field enhancements in the visible and near-infrared (NIR) wavelengths due to their interband transition properties [20]. These properties make gold nanoparticles good candidates for the manipulation of biological materials for a couple of reasons: (1) irradiation by NIR laser light deeply penetrates biological media and (2) gold is a biocompatible material.

As a first step to demonstrate the concept of Plasmonic Laser Nanoablation/Nanosurgery (PLN), we investigate the nanoablation of a solid target by the enhanced plasmonic scattering of ultrafast NIR laser light in the near-field of single, isolated gold nanospheres. Additionally, we believe this study will provide greater understanding in femtosecond laser pulse interactions with gold nanoparticles for solid material modification. The use of femtosecond laser pulses has many distinct advantages [21]: (1) there is a sharp fluence threshold for material modification, which is much lower

than picosecond and longer pulse lengths, (2) the rapid energy deposition allows for efficient and precise ablation with reduced thermal and mechanical defects induced to surrounding regions, and (3) production of well-defined structures in any solid material independent of the excitation wavelength. The use of nanometer-sized gold nanospheres provides many other additional benefits. Particles act as "nanolenses", restricting laser light to the particle's near-field, only photodisrupting material located nanometers away, providing nanoscale resolution, and generating surface structures down to a few tens of nanometers in diameter without the need for a tightly focused laser beam. Moreover, the enhanced electromagnetic field around the particle reduces the amount of required laser fluence for material ablation.

This thesis presents both theoretical and experimental results concerning the ablation of solid materials. Its key objective is to present proof-of-principle experiments and provide an understanding of the basic physical phenomena behind the ablation process. The organization of the thesis is as follows:

Chapter 2: Near-Field Scattering Properties of Noble Metal Particles

In 1908, Gustav Mie presented a full treatment of the Maxwell equations to describe the far-field scattering process by spherical particles. A review of the scattering process will be presented and will be extended into the near-field. Mie theory will be utilized to model the near-field scattering around gold nanoparticles both in a liquid environment and when in contact with a solid medium. Theory shows that there will be large enhancements in the vicinity of the particle.

Chapter 3: Plasmonic Laser Nanoablation of Silicon

To begin our understanding of the plasmonic ablation process, we performed surface ablations on silicon (100) using 150 nm spherical gold nanoparticles and studied generated crater morphology and the minimum fluence required for nanoablation. Silicon is a material having a low overall femtosecond laser ablation threshold similar to one for metal materials such as gold. The crater structure is directly dependent on particle sizes

and laser polarization and fluence. We analyzed nanostructures fabricated by gold nanoparticles irradiated with linearly polarized laser light that was directed in three orientations. Scanning electron microscopy (SEM) and atomic force microscopy (AFM) were used to image ablated nanocraters. Measured near-field enhancements were compared with theoretical values estimated using the solution of the boundary value problem for a spherical particle on a flat semi-infinite substrate.

Chapter 4: Plasmonic Laser Nanoablation of Borosilicate Glass

We next studied the plasmonic ablation process of borosilicate glass using 80 nm spherical gold nanoparticles and studied the role of particle aggregation. Borosilicate glass is a dielectric material having femtosecond laser ablation properties similar to that of biological materials. The crater structure is directly dependent on aggregate size, shape, and orientation to the laser polarization. The technique utilized for both ablation and characterization is identical to that used in the silicon experiment.

Chapter 5: Conclusion and Outlook

The results presented here are only the first steps toward near-field optical processing of materials. With further advances in nanoparticle deposition techniques, this type of ablative technology has the potential to directly impact the fields of laser-assisted nanomachining and nanolithography, providing a patterning method not limited by diffraction and achieving high throughput with reduced production costs. Additionally, the use of antibody specific gold bioconjugates presents the possibility for plasmonic laser nanosurgery, which could be used to manipulate molecules and subcellular structures.

Chapter 2: Near-Field Scattering Properties of Noble-Metal Nanoparticles

The optical cross section for extinction describing light scattering and absorption from an object is most simply defined by [22]:

$$\sigma_{ext} \cong \sigma_{sca} + \sigma_{abs} \tag{2.1}$$

Scattering and absorption events remove energy from the incident light and this attenuation is termed extinction. The electrodynamic (scattering and absorption) phenomenon occurs in all natural materials, so let us begin our discussion with a simple example. A well-known observation is that a blade of grass looks green to the eye. If we inquire why this is the case, we will soon come to the conclusion that green light is more efficiently scattered from the blade of grass to our eye than other colors in the electromagnetic spectrum. In reality, the grass absorbs a large portion of the colors in the visible spectrum; it is for this reason we only perceive the grass as one color. Since this thesis is mostly concerned with noble metals, let us turn our attention to bulk gold. To our eye or a basic optical detector, the bulk gold looks to be a yellow-brown-orange color. By drastically reducing the size of the bulk gold, we will discover a whole host of new material responses that can be exploited for a number of applications. For the remainder of this thesis, we wish to turn our attention to the understanding of the optical responses of nanosized noble metals.

Reducing the size of metallic materials to the nanoscale dramatically affects both the electronic properties and the optical response of the material [22-27]. Changes in material electronic properties occur due to the reduction in the density of states and the spatial length scale of the electronic motion. Energy eigenstates need now to be determined by the material-substrate boundaries, making surface effects of high importance. Optically, as the size is reduced, the extinction becomes size dependent and colors not typically associated with the bulk material can be scattered. Before continuing

on, let us discuss a technological application developed in the Middle Ages. Previously we stated that by reducing the size of bulk gold, we could find a whole host of material responses. This particular application was introduced in the development of the stain glass window. Metallic nanocrystals are responsible for the brilliant reds found in stained glass windows due to the interaction of light with the nano-sized gold particles. Simply by adjusting the size of a gold nanoparticle and the environment in which it is found, it is possible to scatter light at a variety of colors ranging from deep violet to red [28-30]. Figure 2.1 shows this very phenomenom for spherical gold nanoparticles of varying diameter illuminated by a simple light source

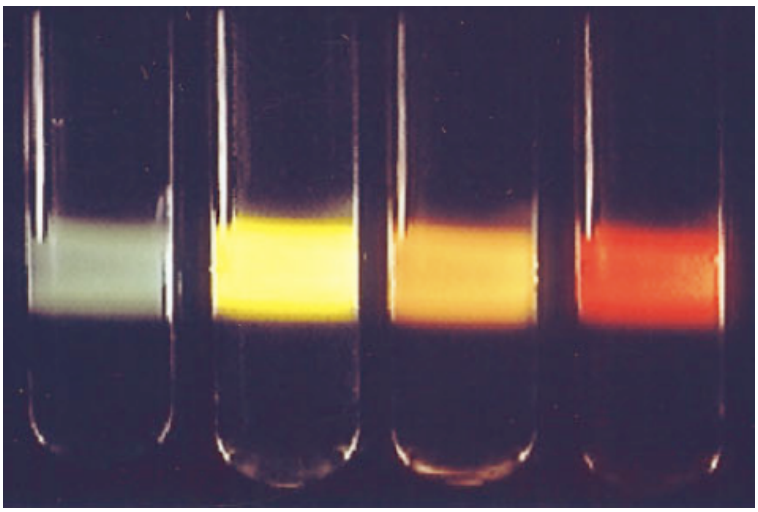

Figure 2.1: Photograph of light scattering from gold nanoparticles. Particle diameter and solution concentration for each shown cuvette are as follows from left to right: 40 nm (1.3×10^{-11} M), 78 nm (1.7×10^{-12} M), 118 nm (5×10^{-13} M), and 140 nm (3×10^{-13} M). Reproduced from [30].

However, understanding of this particular phenomenon is not trivial and a formal solution to the Maxwell equations with the appropriate boundary equations must be realized. Light scattering by nanostructures was first understood by Faraday [31] and in 1908, Gustav Mie was the first to provide a full mathematical treatment [32]. Mie presented a solution to the Maxwell Equations for spherical particles of arbitrary size describing the electrodynamic properties of the particle. Debye furthered Mie's formulation in 1909 and simplified the formulation through additional mathematical

interpretation [33]. It is in this final form of Mie's theory that qualitative generalizations are deduced today.

In this chapter, we discuss the physical properties for the rise of the plasmon resonance and how it affects the electrodynamic properties of a noble-metal nanoparticle. Additionally, the effect of size on the damping and scattering of an electron on the electrodynamic properties will be presented. Finally, a formulization of the scattering and absorption properties of an arbitrarily sized particle in the near- and far-fields will be given.

2.1 Optical Manifestation of Plasmon Resonance

When an optical field is incident a noble-metal nanoparticle, the oscillating electric field perturbs surface conduction electrons. As shown in Fig 2.2, the conduction electrons oscillate coherently with respect to the electric field direction, a phenomenon known as surface plasmon oscillation [34]. This oscillation effect allows noble-metal nanoparticles of a certain size range to strongly absorb and scatter light [21-27]; the surface plasmon resonance is absent in individual atoms as well as in bulk materials. The nature at which the electrons oscillate is dependent upon the particle size and shape; the oscillatory behavior strongly affects particle electrodynamic properties and location and width of plasmon bands.

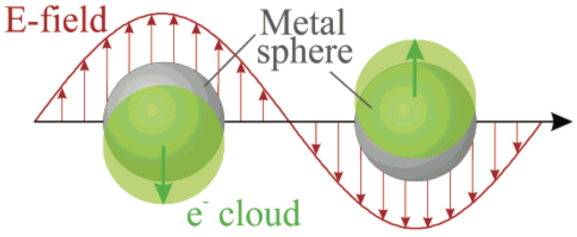

Figure 2.2: Schematic of surface plasmon resonance. Incident electric field displaces conduction electrons relative to the ionic core. Reproduced from [34].

2.1.1 Dipolar Plasmon Resonance in Free-Electron Metals

When the diameter of the charged particle is much smaller than the incident wavelength ($2a << \lambda$), an oscillating dipole field is created. In this case, conduction band electrons

can be well approximated by the Drude free-electron model, which assumes that the conduction band electrons can be treated independently from the ionic core and can move freely, whereas the ions act only as scattering centers [35-37]. As such, conduction band electrons have a higher polarizability and the incident electric field induces a polarization of the electrons with respect to the heavier ionic core. A net charge difference is only felt at the surface of the nanoparticle, creating a restoring force that causes the electron cloud to oscillate in phase in a dipolar fashion.

In this case, retardation effects that lead to plasmon damping are negligible and the extinction cross-section is dominated by dipole absorption, which is described by the following expression [38]:

$$\sigma_{abs}(\omega) = 9\frac{\omega}{c}\varepsilon_m^{3/2}V_0\frac{\varepsilon_2(\omega)}{\left[\varepsilon_1(\omega)+2\varepsilon_m\right]^2+\varepsilon_2(\omega)^2} \tag{2.2}$$

where $V_0 = (4\pi/3)a^3$ is the spherical particle volume, ω is the angular frequency of the excitation radiation, and ε_m and $\varepsilon(\omega) = \varepsilon_1(\omega) + i\varepsilon_2(\omega)$ donate the dielectric functions of the surrounding material and of the particle material, respectively. The absorption resonance is dependent upon the bulk material properties and the position and shape of the resonance is governed solely by the dielectric functions. From Eqn. 2.2, we can deduce that a strong, yet narrow absorption resonance appears at $\varepsilon_1(\omega) = -2\varepsilon_m$ if $\varepsilon_2(\omega)$ is small and does not vary much in the vicinity of the resonance. As is written, size has no effect on the width of the plasmon resonance. We will discuss size parameters further in the next section. Figure 2.3 provides evidence of the optical resonance for a 29 nm silver nanoparticle with respect to wavelength. As is expected, our calculations and experimental data [39] show that the dipolar plasmon resonance at approximately 430 nm wavelength is dominated by absorption. Experimentally, the scattering is negligible. However, our calculations show a small scattering efficiency, which could be do our particle's refractive index not being sized corrected as will be discussed in section 2.1.2.

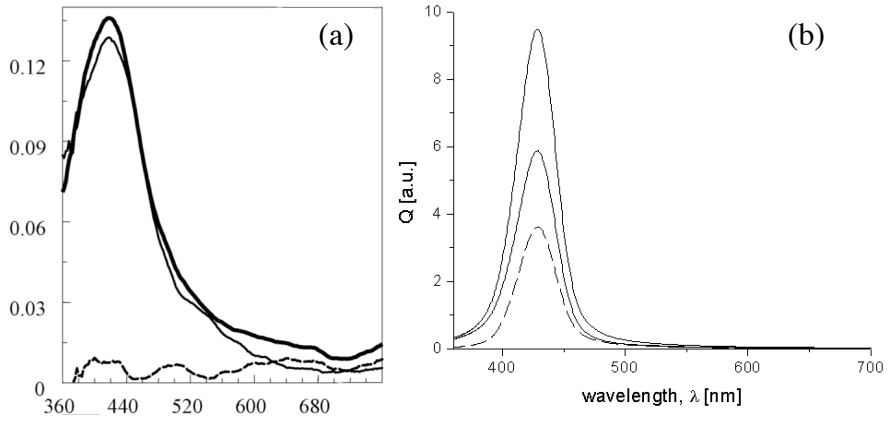

Figure 2.3: (a) Experimental evidence of the optical extinction (solid line), absorption (thin solid line), and scattering (dotted line) for a 29 nm silver particle. Reproduced from [39]. (b) The optical resonance as calculated using Mie Theory.

2.1.2 Size Dependency

Previously, as shown in the description of the dipole approximation, Eqn. 2.2, no size dependency on the width of the plasmon bandwidth was found. Experimentally, in colloidal systems having a weak cluster-matrix interaction, a well-established 1/a size dependency on the plasmon bandwidth has been shown [22,38,40]. Interestingly, there is still controversy surrounding the direction of the shift [40-44]. To account for plasmon width dependency, it has been proposed that the dielectric function needs to directly account for size-dependency [38,45,46]. In free electron metals, the dielectric function is modified by the Drude Model and can thus be found from the following expression:

$$\varepsilon(\omega) = 1 - \frac{\omega_p^2}{\omega^2 + i\gamma\omega} \tag{2.3}$$

where $\omega_p = Ne^2/\varepsilon_0 m_{eff}$ is the plasma frequency and the Drude γ is the phenomenological damping constant. The plasma frequency takes into account the particle's electron density N and the effective electron mass m_{eff}. Assuming the incident light frequency is resonant with the undamped Mie resonance $\omega_1 = \omega_p / \sqrt{(1+2\varepsilon_m)}$, which is only true for free-electron metals, we can rewrite Eqn. 2.2 in terms of the phenomenological damping constant:

$$\sigma_{abs}(\omega) = \sigma_0 \frac{1}{(\omega - \omega_1)^2 + \left(\frac{\gamma}{2}\right)^2} \tag{2.4}$$

In this case, the Drude γ represents the bandwidth of the plasmon polariton in free metal electrons, which does not hold for realistic metals. In realistic metals, the dielectric function must be decomposed into contributions from both interband transitions and the free electron part such that [47]

$$\varepsilon(\omega) = \chi^{free} + \chi^{inter} \tag{2.5}$$

where χ represents the complex dielectric function.

In the classical view of free-electron metals, the scattering of electrons with other electrons, phonons, lattice defects, and impurities leads to damping of the Mie resonance. As the particle size approaches the dimensions of the mean free path of electron scattering, the dimensions of the particle physically limit electron movement, leading to enhanced electron-surface scattering. In gold and silver, the electron mean free path is on the order of 40-50 nm [48]. Additional collision processes result in a reduced electron mean free path and increased damping. It has been found that over the particle diameter range of 2 and 20 nm, the following relationship fits well with experimental data [17]:

$$\gamma(R) = \gamma_0 + \frac{(A\upsilon_F)}{a} \tag{2.6}$$

where A describes the details of the scattering processes, υ_F is the Fermi velocity, and a is the particle radius. To date, A has a variety of theoretical values ranging from 0.1-3.7 [42,43,49-57]. As can be seen, the phenomenological damping relationship now describes the experimentally observed $1/a$ dependence of the plasmon resonance. Because size effects are a function of the particle dielectric function, they are labeled intrinsic size effects [38].

2.1.3 Higher Order Resonance in Free-Electron Metals

As the particle size approaches the incident wavelength, scattering becomes a major contributor. Absorption now becomes directly dependent upon the size of the nanoparticle and is considered an extrinsic size effect. This leads to the extinction being composed of the sum of both absorption and scattering modes. Higher-order multipole electrodynamic effects become more dominant as surface plasmons are unevenly distributed around the particle. As particles increase in size, the incident electric field can no longer homogeneously polarize the surface conduction electrons and retardation effects lead to higher order modes being excited [23]. In this case, the simple dipole approximation becomes no longer valid and the full set of Mie Equations must be solved. Figure 2.4 provides evidence for the evolution of the plasmon resonance with increasing particle size. As is expected, our calculations and experimental results [39] attest to the increased presence of scattering with a larger particle size. Additionally, the plasmon band is now split into two resonances. The dipole resonance has red-shifted to approximately 520 nm wavelength and is dominated by scattering. On the other hand, a new quadrapole resonance appears at the original dipolar resonance of 430 nm and experimentally shows equal degrees of scattering and absorption.

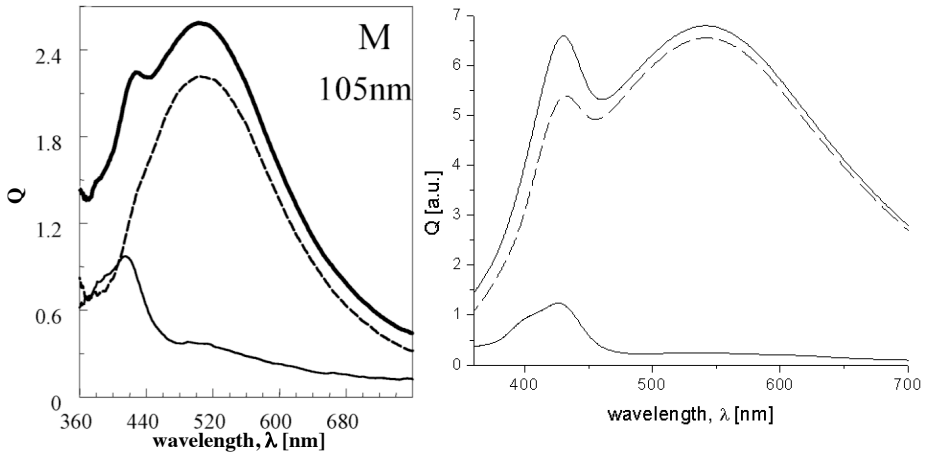

Figure 2.4: (a) Experimental evidence of the optical extinction (solid line), absorption (thin solid line), and scattering (dotted line) for a 105 nm silver particle. Reproduced from [39]. (b) The optical resonance as calculated using Mie Theory.

2.2 Mathematical Treatment

Since the particle radius is much smaller than the wavelength, the electric field component of the incident light, can be taken as constant. This allows us to describe the interaction by electrostatic rather than electrodynamic conditions. In electrostatics, the noble metal's dipole plasma frequency can be easily related to its dielectric constant. To determine the electromagnetic field surrounding a particle, the solution is based on the approach of expanding all electromagnetic waves (incident wave, interior wave, and scattered wave) into spherical partial waves using vector spherical harmonics.

In this section, a mathematical description of the Mie formulation using Poynting's Theorem will be presented. The treatment will be subjected to a few limitations:

(a) Coherent scattering - light scattered from the particle is of the same frequency as the incident light.

(b) Independent scattering – the homogeneous medium of refractive index n_0 in which the nanoparticles are embedded is not highly scattering.

(c) Single scattering - spherical particles of radius a much smaller than the optical wavelength λ are well isolated. The effects of multiple scattering are neglected.

2.2.1 Far-Field Efficiencies

In our derivation, we consider a spherical particle of diameter $2a$ and size dependent refractive index $m = \sqrt{\varepsilon_1(\omega)/\varepsilon_m}$, which is the ratio of the vacuum refractive index to the medium refractive index. Illumination is by a plane wave propagating along the z-axis, polarized along the x-axis, and of vacuum wavelength λ. The particle is embedded in a nonabsorbing host medium.

Assuming the resultant electromagnetic field outside the sphere results from the superposition of the incident field and scattered fields, we can determine the power rate for absorption:

$$W_{abs} = W_0 + W_{ext} - W_{sca} \tag{2.7}$$

Here W_0 is the rate of energy absorption in the medium, W_{ext} the extinction rate, and W_{sca} the scattering rate. Applying Poynting's theorem, $S = 1/2\mathrm{Re}\left(E \times H^*\right)$, to the rate equation, we find:

$$\begin{aligned} W_{abs} = &-\frac{1}{2}\mathrm{Re}\int_0^{2\pi}\int_0^{\pi}\left(E_{inc} \times H_{inc}^*\right)e_R R^2 \sin\theta d\theta d\varphi \\ &-\frac{1}{2}\mathrm{Re}\int_0^{2\pi}\int_0^{\pi}\left(E_{inc} \times H_{sca}^* + E_{sca} \times H_{inc}^*\right)e_R R^2 \sin\theta d\theta d\varphi \\ &-\frac{1}{2}\mathrm{Re}\int_0^{2\pi}\int_0^{\pi}\left(E_{sca} \times H_{sca}^*\right)e_R R^2 \sin\theta d\theta d\varphi \end{aligned} \tag{2.8}$$

Here Re indicates the real part and the asterisk the complex conjugate. Since the embedding medium is nonabsorbing, W_0 vanishes since no energy will be lost to the surrounding medium. The rate equation is now normalized by the incident wave intensity I_0 to obtain the optical cross section, σ_{abs}. Since it is more practical to express the electrodynamic properties of the nanoparticles in terms of a nondimensional efficiency terms, the cross section is normalized against the geometrical cross section $2a$ of the spherical particle, giving:

$$Q_{abs} = \frac{\sigma_{abs}}{\pi a^2} \tag{2.9}$$

In turn, the scattering and extinction efficiencies, which are more important to the present work, are related to the absorption efficiency by the following relation:

$$Q_{abs} = Q_{ext} - Q_{sca} \tag{2.10}$$

At this point, all electromagnetic fields contained within the absorption expression are expanded according to their vector spherical harmonics. The solution is developed according to two boundary conditions, which are applied to solve for the unknown expansion coefficients of the scattered and interior wave: (1) the electric potential is continuous at the sphere surface and (2) the normal component of the electric displacement is also continuous. All expanded fields are inserted back into Eqn. 2.8 and it is then integrated along a finite 2R region located in the particle far-field, R >> a. To keep the solution relatively simple, Debye introduced the Riccati-Bessel function $\psi_n(kR)$ and a Riccati-Hankel function $\zeta_n(kR)$ [33]. The separated extinction and scattering efficiencies given in explicit form are:

$$\begin{aligned} Q_{ext}(R) &= \frac{2}{x^2}\sum_{n=1}^{\infty}(2n+1)\mathrm{Re}(a_n+b_n) \\ &\times \mathrm{Im}\left(\zeta_n(kR)\psi_n'(kR)^* - \zeta_n'(kR)\psi_n(kR)^*\right) + \mathrm{Im}(a_n+b_n) \\ &\times \mathrm{Re}\left(\zeta_n(kR)\psi_n'(kR)^* - \zeta_n'(kR)\psi_n(kR)^*\right) \end{aligned} \tag{2.11}$$

$$Q_{sca} = \frac{2}{x^2}\sum_{n=1}^{\infty}(2n+1)\left\{|a_n|^2 + |b_n|^2\right\} \times \mathrm{Im}\left(\zeta_n(kR)\zeta_n'(kR)^*\right) \tag{2.12}$$

where $x = ka$ is the size parameter and $k = 2\pi m/\lambda$ is the wavenumber outside the particle. a_n and b_n are the scattering coefficients of the sphere, given by:

$$a_n = \frac{\psi_n'(mx)\psi_n(x) - m\psi_n(mx)\psi_n'(x)}{\psi_n'(mx)\zeta_n(x) - m\psi_n(mx)\zeta_n'(x)} \tag{2.13}$$

and

$$b_n = \frac{m\psi_n'(mx)\psi_n(x) - \psi_n(mx)\psi_n'(x)}{m\psi_n'(mx)\zeta_n(x) - \psi_n(mx)\zeta_n'(x)} \tag{2.14}$$

Using the relationship $\zeta_n(kR) = \psi_n(kR) + i\chi_n(kR)$, where χ_n is a Riccati-Neumann function, Eqn. 2.11 and 2.12 can be written in terms of χ_n. Since all solutions of kR will

be real for which the Neumann and Bessel functions are real, the following statement can be made:

$$\zeta_n'\psi_n'^{*} - \zeta_n'\psi_n^{*} = -i\left(\chi_n\psi_n' - \psi_n\chi_n'\right) \tag{2.15}$$

Independent of kR, the value of the Wronskian of real functions will always equal 1. Using the same line of reasoning, $\mathrm{Im}\left(\zeta_n\zeta_n'^{*}\right) = 1$ for all kR. This allows then for Eqn. 2.11 and 2.12 to be reduced to [58]:

$$Q_{ext} = \frac{2}{x^2}\sum_{n=1}^{\infty}(2n+1)\mathrm{Re}\left(a_n + b_n\right) \tag{2.16}$$

and

$$Q_{sca} = \frac{2}{x^2}\sum_{n=1}^{\infty}(2n+1)\left\{\left|a_n\right|^2 + \left|b_n\right|^2\right\}, \tag{2.17}$$

Q_{ext} and Q_{sca} provide a measure for the ability of sphere to extinct and scatter an incident electromagnetic wave λ. No information about the actual strength of the electromagnetic field near or far from the particle can be deduced. The efficiencies provide a nice measure to understand the electromagnetic property of interest with respect to wavelength. As shown in Fig 2.5, we examined the effect of size on a gold nanoparticle's extinction spectra. With increasing particle diameter 2a the extinction peak redshifts, the magnitude of the resonance reduces, and the resonance width broadens considerably. Additionally, the excitation of higher order modes becomes visible at the larger particle diameters.

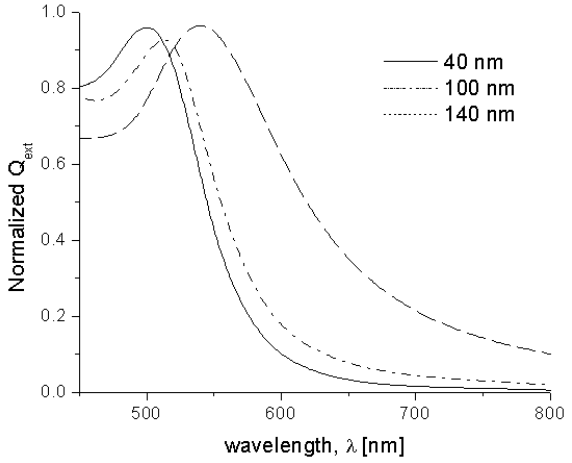

Figure 2.5: Normalized Mie extinction spectra of gold nanospheres for increasing particle diameters (2a). The extinction was calculated using the relation 2.17.

In the next section we will discuss a new efficiency term, which can be directly linked with the electromagnetic field strength.

2.2.2 Near-Field Efficiencies

In many common applications and experimental conditions, measurements of light scattering are made in the far field zone, i.e. a distance far away from the particle surface. Far-field parameters such as the extinction coefficient, consist solely of the electric field components E_θ and E_ϕ. As we move our point of interest close to the vicinity of the particle, we will find a rapid increase in the local electromagnetic field, which is due to the addition of the radial electric field component E_R. This is verified in the known fact that for free-electron metals, the electric field must radiate normally to the surface. To describe the strength of the electromagnetic field in the near-field regime, Messinger *et al*. introduced the following term [59]:

$$Q_{NF}(R) = \frac{R^2}{\pi a^2} \int_0^{2\pi} \int_0^{\pi} E_S \bullet E_S^* \sin\theta d\theta d\phi \tag{2.18}$$

and

$$Q_R(R) = \frac{R^2}{\pi a^2} \int_0^{2\pi} \int_0^{\pi} E_R \bullet E_R^* \sin\theta d\theta d\phi \tag{2.19}$$

Q_{NF} represents the square of the spatially averaged electric field of the scattered wave $E_S = \left(E_R, E_\theta, E_\varphi\right)$ as a function R. The scattered field consists of all three components of the electric field vector, where the angular components, E_θ and E_φ, are perpendicular to the particle surface and the radial component, E_R, lies normal to the surface. It provides a measure for the ability of the sphere to convert the incident electric field intensity to a near-field intensity. Q_R is the contribution of Q_{NF} due to the radial field component only and provides a measure of the sphere's ability to convert the incident electric field into a radially directed field. As Fig. 2.6 shows, the main contribution of scattering in the near-field, approximately 67%, is the radial electric field component. Because the E_R field component increases proportionally to R^{-2}, Q_{NF} will increase fast than Q_{sca}, which is only proportional to R^{-1}. As $R >> a$, Q_{NF} will approach the asymptotic value of Q_{sca}. Figure 2.6 provides a theoretical plot of the near-field components in relation to the far field scattering for a gold particle of 2a = 100 nm as found from Quinten [60].

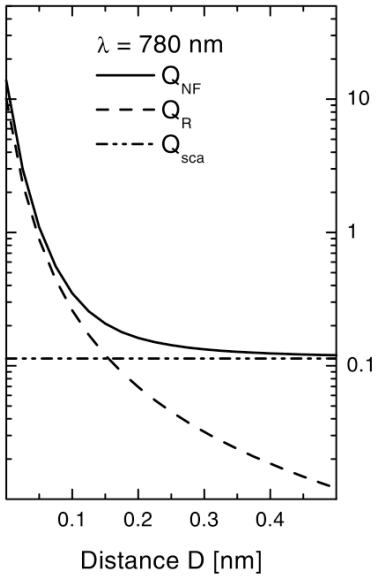

Figure 2.6: Dependence of the near- and far- scattering effiencies on the distance from the particle surface. Reproduced from [60].

The explicit calculations of Q_{NF} and Q_R yield the following expression in terms of the scattering coefficients of a sphere at the particle surface (R = a):

$$Q_{NF} = 2\sum_{n=1}^{\infty}\left\{|a_n|^2\left[(n+1)\left|h_{n-1}^{(2)}(ka)\right|^2 + n\left|h_{n+1}^{(2)}(ka)\right|^2\right] + (2n+1)|b_n|^2\left|h_n^{(2)}(ka)\right|^2\right\} \tag{2.20}$$

and

$$Q_R = \frac{2}{x^2}\sum_{n=1}^{\infty}(2n+1)(n+1)n|a_n|^2\left|h_n^{(2)}(ka)\right|^2, \tag{2.21}$$

where $h_n^{(2)}$ is the Hankel function of the second kind. In this form, Q_{NF} provides us a measure of the relative near-field intensity as a function of particle size and incident wavelength. The above formulation of the near- and far-field efficiencies provides a complete picture of the scattering and absorption properties of an individual sphere of arbitrary size.

2.3 Role of Absorption and Scattering in Plasmonic Laser Nanoablation

Depending upon the desired application, nanoparticle geometry and size can be tuned to obtain a wide range of absorption and scattering resonances ranging from the visible to the near-infrared. From our earlier discussion, for spherical particles, we find that absorption dominates the dipolar resonance for smaller particle sizes, while scattering gains greater importance with increasing particle size. With increasing particle size, we find that both the absorption and scattering components of the plasmon band red-shift. However, the absorption peak stops red-shifting when it reaches the wavelength of approximately 600 nm, beyond which it drops off to negligible amounts. The drop off in absorption is due to the dielectric function of gold reducing with longer wavelengths due to reduced *d*-level to *sp*-band electronic transitions, giving significantly reduced absorption effects. For scattering-based applications, this drop-off effect in the absorption is desirable for near-infrared, pulsed laser systems. In contrast, absorption-based applications using spherical particles (other particle shapes, i.e. rods, red-shift the

absorption band into the near-infrared) require wavelengths centered in the visible wavelength range. When observing the near-field scattering, we find that there is a continued red-shifting in the scattering plasmon band deep into the near-infrared. Using this information, we can engineer a particle size complementary to our desired plasmonic scattering ablation effect.

Specifically in our ablation technique, we wish to reduce the degree of absorption of the incident energy by the particle, while largely increasing the scattering in the particle near-field. It is of upmost importance to remember that as the near-field red-shifts, the magnitude of the plasmon band decreases and the plasmon width broadens.

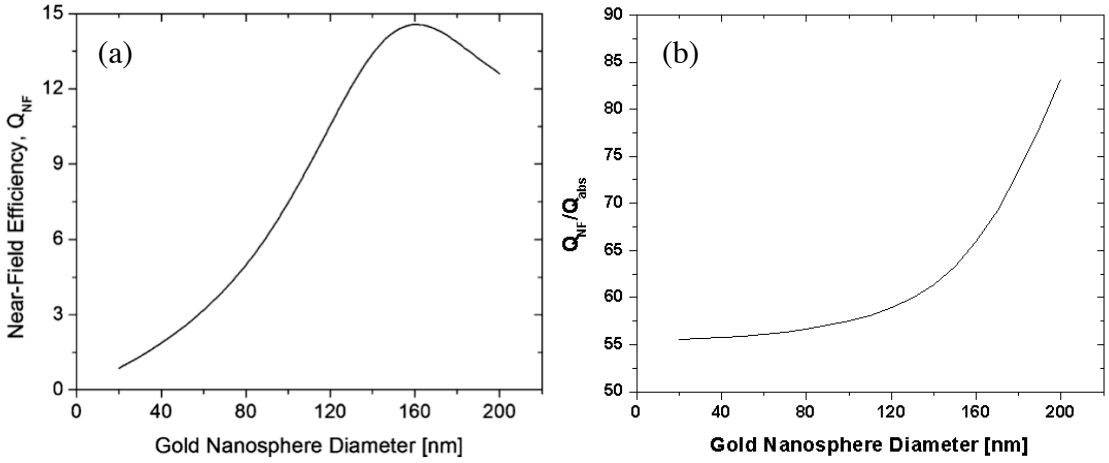

Figure 2.7: (a) Estimated near-field scattering efficiency, Q_{NF}, of gold nanospheres in air as a function of particle diameter at 780 nm excitation wavelength. Q_{NF} is a measure of the particle's ability to convert incident electric field intensity into a near-field intensity. The efficiency term was estimated using Eqn. 3.3 according to [59]. (b) Ratio of Q_{NF} to Q_{abs} of gold nanospheres as a function of particle diameter at 780 nm excitation wavelength.

Most likely it will not be desirable to have the near-field scattering peak centered at the incident laser wavelength. Figure 2.7a summarizes the calculations of Q_{NF} using Eqn. 2.21. The plot indicates that the near-field enhancement of a spherical gold particle in air is greatest for particles 150–170 nm in diameter at the 780 nm wavelength. While having a larger near-field enhancement, 150 nm particles have greatly reduced absorption effects. Using the ratio of the near-field scattering to the absorption efficiency, $\zeta = Q_{NF}/Q_{abs}$, we can determine how suitable the particle is for scattering applications.

Figure 2.7b provides a plot of this ratio over a range of particle diameters. As the particle diameter increases, the degree of near-field scattering rapidly increases over the absorption at the 780 nm wavelength. A 150 nm particle in a medium of air scatters 65 times more incident energy in the particle near-field than it absorbs it. Since 150 nm gold particles exhibit large scattering properties in the near-field with minimal absorption effects, they are excellent candidates for plasmonic ablation.

Chapter 3: Plasmonic Laser Nanoablation of Silicon

We first demonstrate the fabrication of nanostructures ablated on silicon (100) by the plasmonic scattering of 780 nm, 220 fs laser pulses in the near-field of gold nanospheres. We take advantage of the enhanced plasmonic scattering of ultrashort laser light in the particle near-field to ablate well-defined nanocraters. Gold nanospheres of 150 nm diameter are deposited onto a silicon surface and irradiated with a single laser pulse. We studied the effect of laser polarization on the morphology of ablated nanostructures and estimated the minimum fluence for plasmonic nanoablation. When the polarization of the incident radiation is directed at a 45° angle into the substrate surface, a near-field enhancement of 23.1 ± 7.6 is measured, reducing the required silicon ablation fluence from 191 ± 14 mJ/cm^2 to 8.2 ± 2.9 mJ/cm^2. Enhancements are also measured for laser polarizations parallel to the substrate surface when the substrate is angled 0° and 45° to the incident irradiation, giving enhancements of 6.9 ± 0.6 and 4.1 ± 1.3, respectively. Generated nanocrater morphologies show a direct imprint of the particle dipolar scattering region, as predicted in our theoretical calculations. The measured near-field enhancement values agree well with the maximum field enhancements obtained in our calculations. The agreement between theory and measurements supports that the nanocraters are indeed formed by the enhanced plasmonic scattering in the near-field of the nanoparticles.

3.1 Experimental Setup

Figure 3.1 illustrates the experimental setup. A femtosecond Ti:sapphire laser system (Spitfire, Spectra Physics, Mountain View, CA) delivered laser pulses of 220 fs temporal width and 780 nm wavelength at a 1 kHz repetition rate. An attenuator consisting of a half-wave plate and a polarizing cube beam-splitter was used to control the delivered laser power. Pulse energies were measured before the focusing system using an energy

meter (Ophir PL10). The measured pulse energy transmission through the focusing system was estimated to be 64% by finding the ratio of energy before and after the objective. The sample was mounted onto an *x*-*y* translational stage. The setup provided simultaneous optical imaging and ablation of the sample through the same objective lens.

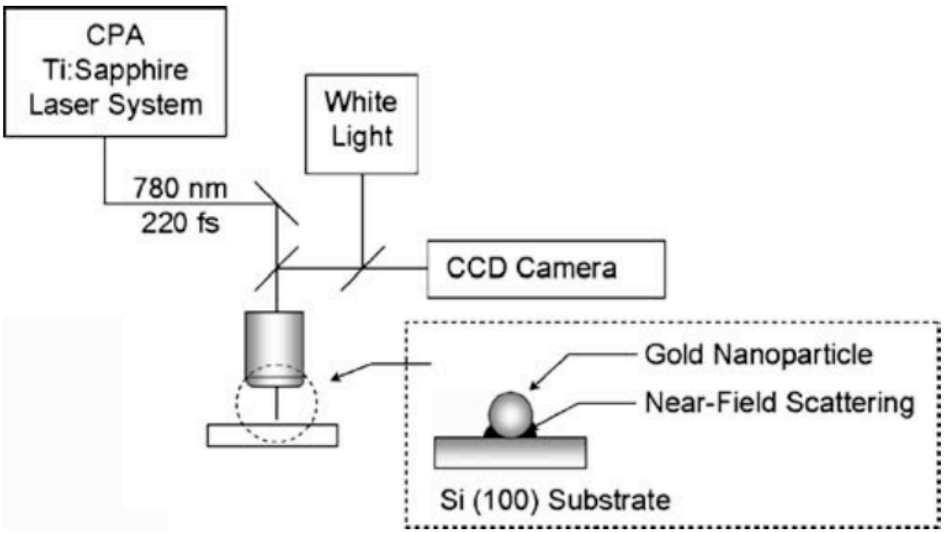

Figure 3.1: Schematic of the femtosecond laser ablation system.

We used a long working distance objective lens (0.28 NA, 10 x; Mitutoya) to focus a linearly polarized laser pulse to a $1/e^2$ radius of 3.2 ± 0.2 μm at the beam waist. In plasmonic ablation experiments, the sample was placed 80 μm from the beam waist to obtain a larger spot size. The spot size at this location was estimated based on the linear dependence of the ablation crater diameter, D, with respect to the logarithm of laser energy E_{pulse} [61],

$$D^2 = 2w_0^2 \ln\left(\frac{E_{pulse}}{E_{pulse,th}}\right) \tag{3.1}$$

Here, w_0 is the $1/e^2$ Gaussian beam radius and $E_{pulse,th}$ is the pulse energy when $D = 0$. Figure 3.2 plots the diameter of the ablation craters on silicon measured using SEM for various incident laser energies and corresponding fluences. By estimating the slope of

the linear fit to the data points, w_0 was determined. At the ablation plane (z = 80 μm), the beam was elliptically shaped such that the measured 1/e^2 short axis radius was w_{0x} = 11.1 ± 0.3 μm and the long axis was w_{0y} = 11.8± 0.2 μm. The beam ellipticity is attributed to the astigmatic focusing properties of the beam, where the x and y directions of the beam have different focal planes. To determine the quality of the beam in each axis, the relative "M-squared" value was calculated using the following relationship:

$$w(z) = w_0\sqrt{1+\left(\frac{z}{z_R}M^2\right)^2} \tag{3.2}$$

where z_R is the Rayleigh range, z is the distance of propagation, and M^2 is the beam quality. From Eqn. 3.2, we find $M_x^2 \approx$ 1.73 and $M_y^2 \approx$ 1.84, where M_x^2 and M_y^2 correspond to the beam quality in the x and y directions, respectively. Through the direct imaging of optically induced surface changes, this technique provides a precise method for finding laser spot sizes with minimal uncertainties. Measurement uncertainties arise in the curve-fitting algorithm and in pulse-to-pulse energy variability of 5%. To obtain a homogeneous, well-defined energy distribution on the target, a circular aperture (6.5mm in diameter) was placed in the beam path just before the objective. The spatial profile of the truncated beam, originally 8 mm in diameter, was not significantly modulated at the sample plane [62]. All experiments are performed in air at atmospheric pressure.

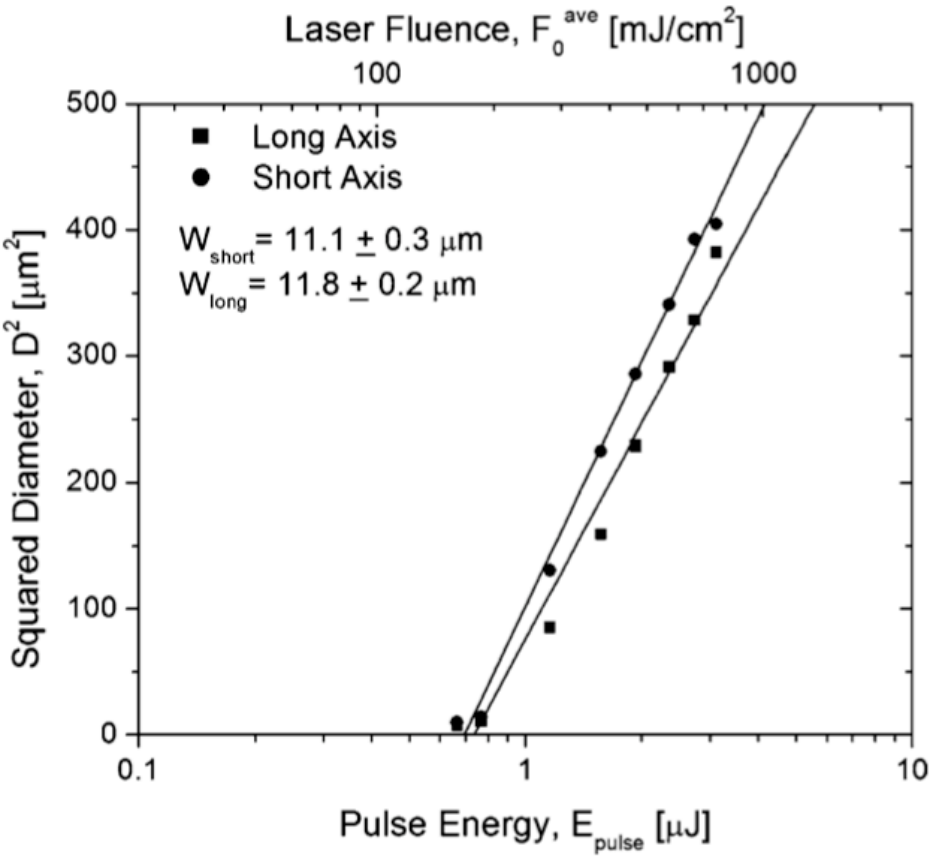

Figure 3.2: The squared diameter of the laser-induced damage on the silicon is plotted as a function of the laser fluence. The slope of the linear fit provides the $1/e^2$ Gaussian beam waist at the plane of ablation. The modification region (i.e., the full extent of damage to the silicon surface due to the irradiation by a single laser pulse) was measured using SEM.

The orientation of the laser polarization at the sample plane was varied through the manipulation of the sample. When the laser light was directed to be orthogonal to the sample, the laser polarization was parallel to the substrate surface. For the laser to be directed at a 45° angle with respect to the silicon surface, the substrate was mounted onto a standard 45° angle SEM block. By rotating the angled sample 90°, the electric field was either oriented into (*p*-polarized laser light) or along (*s*-polarized laser light) the surface plane. The size of the ellipticity of the irradiation zone was modulated as the sample was angled with respect to the laser. The axis of the beam that was aligned along the angled sample plane was lengthened by a factor $\sqrt{2}$.

3.2 Sample Preparation and Characterization

A silicon (100) wafer (bandgap energy of 1.14 eV) having a 21 Å native oxide layer as measured by ellipsometry was cut into a 5 x 5 mm piece and washed using a four step process: sulfuric acid, distilled water, acetone, and methanol. The wafer was ultrasonicated in each solution for 5 min and stored in methanol until use. A 6 μL aliquot of colloidal gold (2R = 150 nm; British Biocell International) was deposited onto the surface. The colloidal gold solution was prepared via the citrate reduction of hydrochloric acid. The sample was annealed in air at 120 °C for 5 min. By using this method, isolated particles could be deposited on the substrate surface.

Before and after irradiation, samples were characterized using SEM (LEOS 1530) and AFM (Dimension 3100; Digital Instruments). The AFM was operated in tapping mode in air using triangular shaped silicon cantilevers (40.0 N/m spring constant and 300 kHz resonance frequency; Budget Sensors).

3.3 Theoretical Considerations in Choosing the Nanoparticle Size

To determine the appropriate particle size to produce the largest field enhancement at 780 nm, we estimated the near-field scattering efficiency, Q_{NF}, of a gold particle embedded in air as a function of its radius. We solved for Q_{NF} at the particle surface using the following expression [59]:

$$Q_{\mathrm{NF}} = \frac{R^2}{\pi a^2} \int\int E_s E_s^* \sin\theta d\theta d\varphi \Big|_{R=a} \tag{3.3}$$

where R defines a spherical surface over which the integral is evaluated and a is the particle radius. For a given set of sphere parameters, Q_{NF} will be greater than unity, which implies the sphere acts as a field intensifier. This yields local fields larger than that incident on the particle. Previously, in Fig. 2.7 we summarized the calculations using Eqn 3.3 for a spherical gold particle of varying diameter at the incident wavelength of 780 nm. The plot indicates that the near-field enhancement of a spherical gold particle

in air is greatest for particles 150–170 nm in diameter at the 780 nm wavelength. Since we previously show that a 150 nm gold particles exhibits large scattering properties in the near-field with minimal absorption effects, we will utilize that particle size for our silicon experiments.

3.4 Femtosecond Laser Ablation of Silicon

Silicon is a material having a low overall femtosecond laser ablation threshold similar to one for metal materials such as gold. A common method for estimating the single-shot ablation threshold of silicon (100) $F_{abl,th}$ is through the linear relationship between the ablation depth h_a and the average fluence F_0^{ave} [61,62]:

$$h_a = \alpha_{eff}^{-1} \ln\left(\frac{F_0^{ave}}{F_{abl,th}}\right) \tag{3.4}$$

where α_{eff}^{-1} is the effective optical penetration depth and $F_{abl,th}$ is the pulse fluence when h_a = 0. Figure 3.3 presents the ablation depth data measured using AFM for corresponding laser fluences. By extrapolating the linear fit to zero, we find the single-shot ablation threshold of silicon to be $F_{abl,th}$ = 191 ± 14 mJ/cm^2. Uncertainty in the ablation threshold measurement arises mainly due to the error in the measured spot size and pulse-to-pulse energy variability.

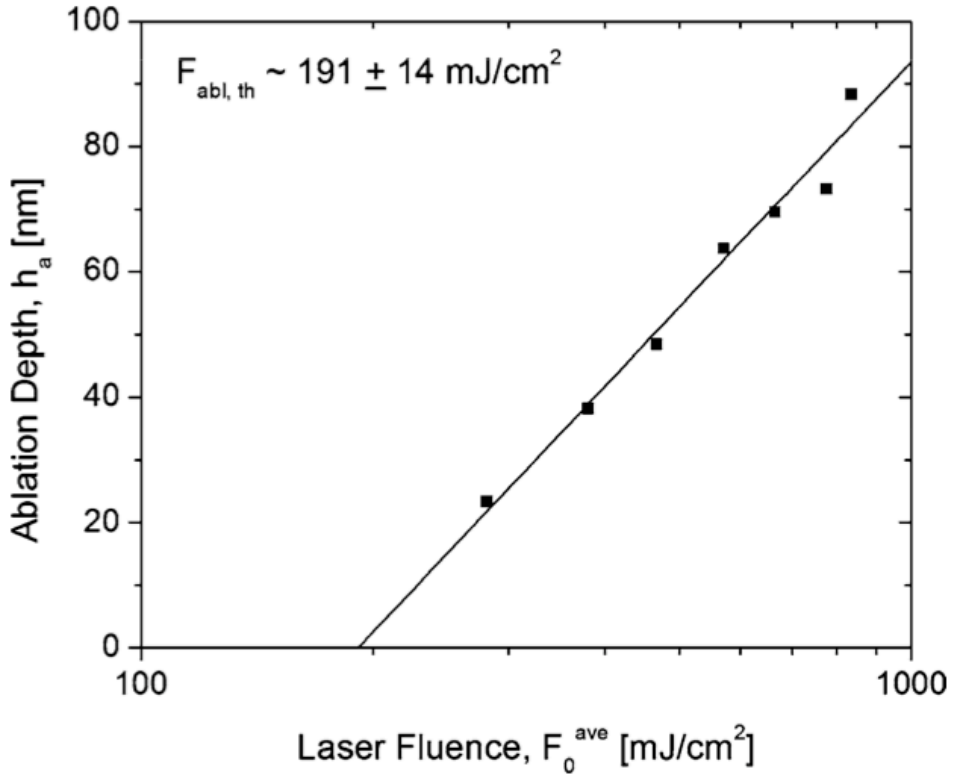

Figure 3.3: The depth of the laser ablated silicon crater is plotted as a function of the laser fluence. Extrapolation of the linear fit to zero provides the single-shot femtosecond laser ablation threshold of silicon.

Ablation craters generated at laser fluences lower than about 1 J/cm^2 are mediated by the optical penetration depth [63]. In Fig. 3.3, we only present results within this regime. At 780 nm wavelength, the dominant mechanism of electron excitation is single photon absorption due to the photon energy (1.6 eV) having greater energy than the silicon bandgap (1.14 eV) [64]. Since absorption is linear, the ablation profile will resemble the intensity distribution of the incident light. As the laser fluence is increased above 1 J/cm^2, thermal effects begin to affect the surrounding lattice. Carrier conduction contributions become important and the electron-driven heat penetration depth defines the ablation depth.

Before the onset of true ablation, i.e. removal of material, irradiation of silicon with a low fluence laser pulse can result in surface modification. Below the ablation threshold the molten layer will resolidify either into an amorphous or re-crystallized state.

The amorphous region marks the lowest input energy needed to achieve modification. The molten layer re-solidifies faster than the re-crystallization time scale, leaving it in an amorphous state [65]. The single shot modification threshold for silicon (100) was estimated to be about 186 mJ/cm^2. This threshold was determined from the data presented in Fig. 3.2, where the linear fit was extrapolated to zero.

3.5 Effects of Gold Nanoparticles on Silicon Ablation

Figure 3.4a shows an SEM image of a nanoparticle studded silicon (100) wafer after irradiation by an elliptically shaped laser pulse of 190 mJ/cm2 average fluence. In Fig. 3.4b, a Gaussian curve representing the peak incident fluence along the short axis is given as a reference to the different ablation regimes along the irradiation zone. The spatial profile of a Gaussian beam is given by:

$$F(r) = F_0^{peak} \exp\left(-\frac{2r^2}{w_0^2}\right) \tag{3.5}$$

where F_0^{peak} is the peak laser fluence and r is the distance from beam center. Typically the fluence is given in terms of an average value instead of the peak fluence, as is such in this text. The average fluence can be determined by:

$$F_0^{ave} = \frac{E_{pulse}}{\pi w_0^2} \tag{3.6}$$

The incident pulse was directed such that it was orthogonal to the substrate surface with the **E**-field along the short axis of the elliptical pulse. The application of a laser pulse having a Gaussian intensity distribution allows for a broad range of laser fluences to be studied in a single experiment. Several identifiable regions of surface modification are observable. In increasing distance from irradiation center these regions are:

1. *Amorphization of Si(100):* In the center, there is a region of surface modification due to the amorphization of Si (100). In this region, no material

is removed from the substrate, which is confirmed with AFM. The surface roughness, however, increases to about 5 nm. Amorphization occurs until the laser fluence drops to approximately 176 mJ/cm^2, which agrees with the modification threshold stated earlier in the paper. All particles in this region are completely ablated and any plasmonic effect is washed out due to long silicon melt times.

2. *Ablation induced by local enhancement near the particles:* Here we observe a region of surface ablation on the micronscale induced by the laser enhancement in the near-field of the particles. The ablation craters are surrounded by a region of surface melt. Generally, rim structures and splash zones border the melt zones. Again, particles are completely ablated at this laser fluence level.
3. *Ablation at the nanoscale via local enhancement near the particles:* The enhancement in the vicinity of the particles generates nanoscale craters on the silicon surface that are direct imprints of the dipolar scattering pattern with any surrounding damage to the silicon lattice. Here, the laser fluence is not large enough to completely ablate the particle. The collective oscillations of electrons (surface plasmons) in the nanoparticle cause the particle to split into two halves as will be shown later in the paper. The molten gold generally resolidifies at the outer edges of the ablation crater. In the case of plasmonic ablation for nanolithography applications, it would be ideal to work in this fluence level. Material removal only extends tens of nanometers from the particle center and is confined to the nanoscale.
4. *No surface modification/ablation:* The incident laser fluence continues to decrease such that the local enhancement generated by the particle is not enough to overcome the modification threshold of the silicon substrate. As described later in the paper, this ablation limit occurs at an average fluence of 27.5mJ/cm^2, when the laser polarization is oriented parallel to the silicon surface. Beyond this point, both silicon and gold remain intact.

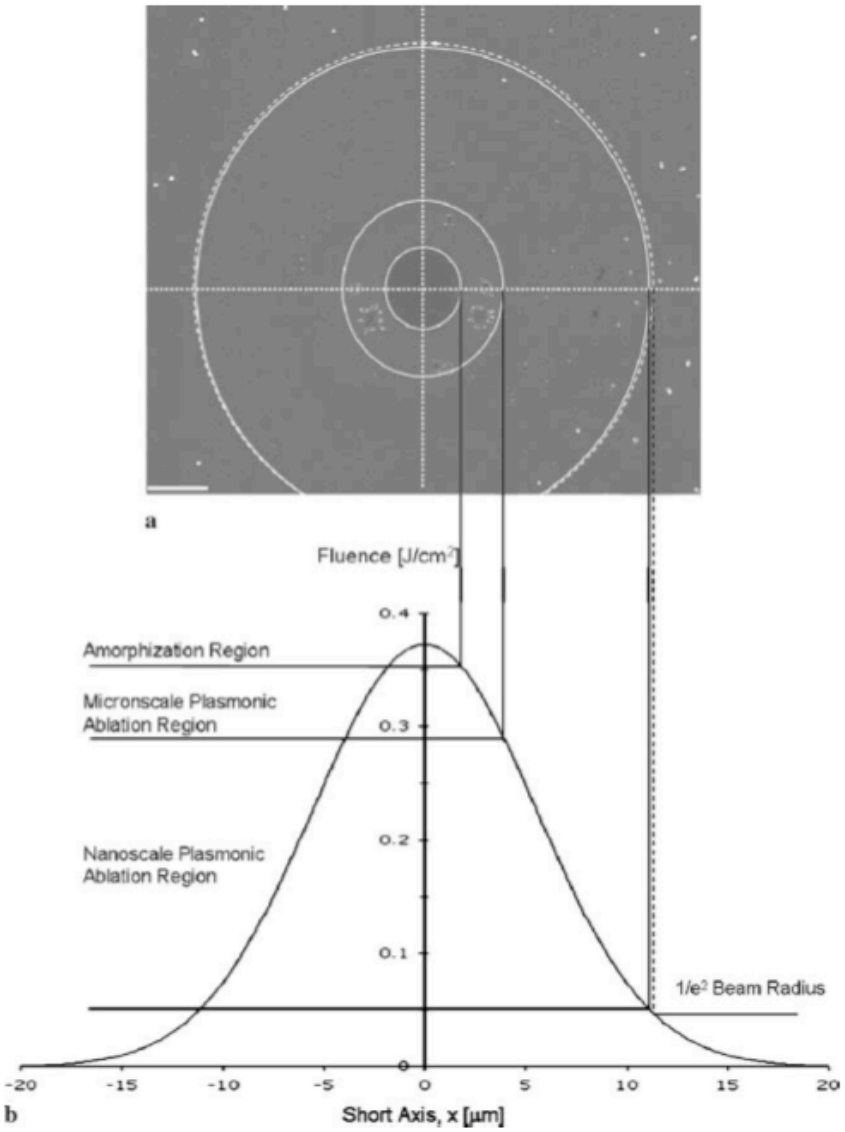

Figure 3.4: An SEM image of nanoparticles deposited on silicon substrate after laser irradiation (a) and the corresponding Gaussian distribution of the laser beam (b). A 190 mJ/cm^2 average fluence is directed orthogonally to the substrate (normal incidence). Several regions of ablation can be ascertained from the image. The *scale bar* is 3μm.

3.6 Ablation Threshold of Gold Nanoparticles

We determined the gold nanoparticle ablation threshold to be between 20 to 25 mJ/cm^2, which we define as the laser fluence below which the whole spherical structure of the particle remains intact. This value is in good agreement with the recently reported damage threshold value of 15.5 mJ/cm^2 for nanospheres of 38 nm in diameter irradiated

by 400 nm, 100 fs laser pulses [66]. In those studies, picosecond X-ray scattering measurements revealed that partial material removal from the poles of the nanoparticle occurs for fluences above 15.5 mJ/cm^2. Below 20–25 mJ/cm^2, we may expect some material removal to occur, reducing the overall size of the particle in regions of intense scattering. In cases where the plasmonic ablation threshold of silicon is lower than the ablation threshold of the gold particle, nanocrater structures may form underneath the particle itself for fluences down to the threshold value.

3.7 Effects of Laser Polarization on Nanocrater Morphology

We studied the effect of laser polarization on the morphology of ablated nanostructures. Figure 3.5 presents AFM images and cross-sectional profiles of the nanocraters obtained using different cases of laser polarizations. In each case, the scattering patter in the particle near-field was directly imprinted into the silicon. When the radiation E-field is directed at a 45° angle into the silicon substrate surface (p-polarized light), only one lobe of the dipolar scattering region interacts with the underlying substrate, leading to the formation of a single circular crater. In Fig. 3.5a, the relative fluence interacting with the particle, was 88 mJ/cm^2. A crater having a 100 nm diameter and 53 nm maximum depth was generated. Images of the craters produced by laser polarizations parallel to the substrate surface when the substrate is angled 0° and 45° to the incident irradiation (s-polarized laser light) are shown in Fig. 3.5b-c, respectively. In each of the cases, when the laser polarization is parallel to the substrate surface, the generated craters have a double lobed crater structure, which follows the dipolar scattering pattern of the nanoparticle. Resolidified gold can be found at the ends of each dipolar crater. In Fig. 3.5, the gold can be clearly visualized and is represented as the peak(s) surrounding the craters in the cross-sectional profiles.

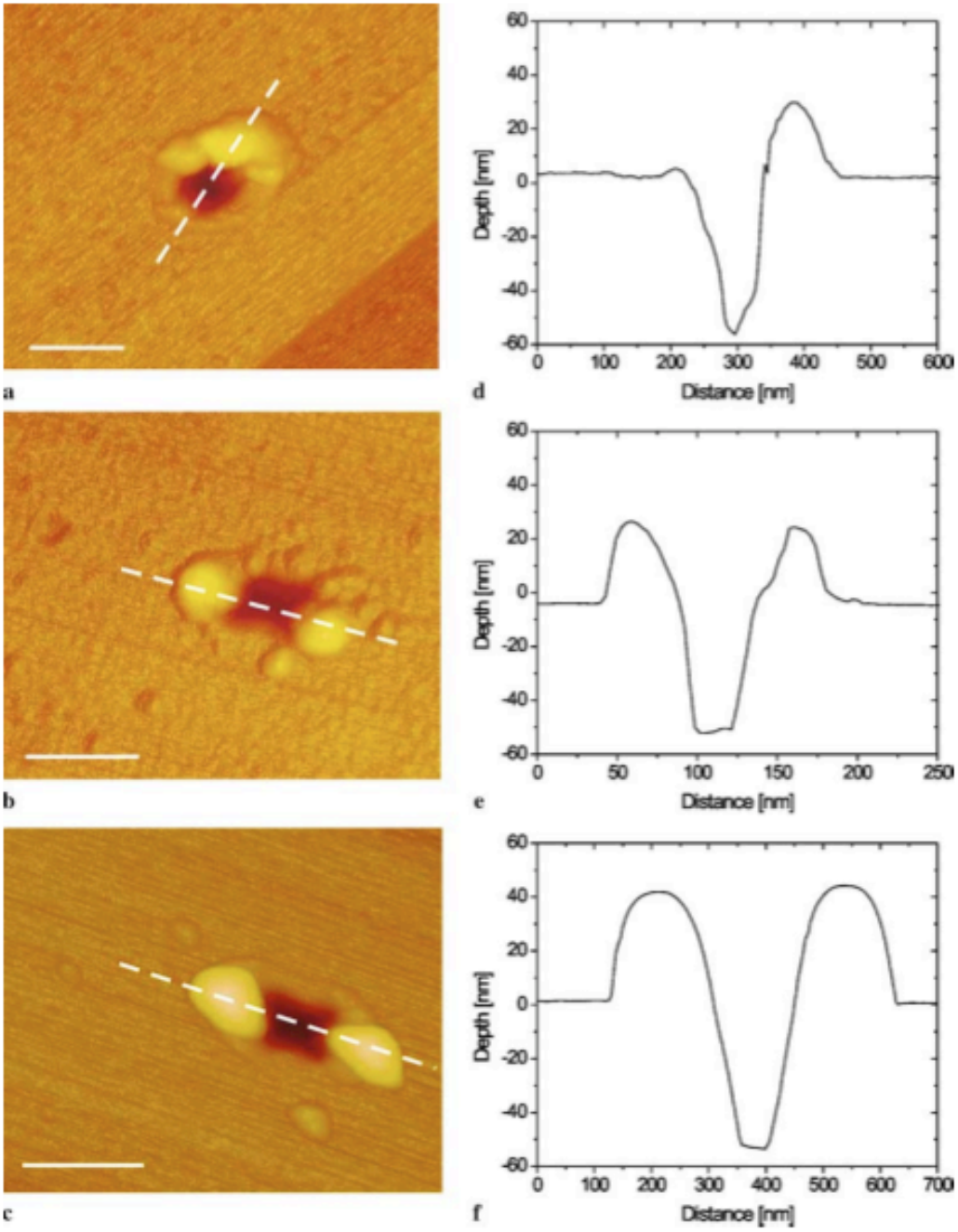

Figure 3.5: AFM images of nanocraters ablated by 150 nm gold nanoparticles on silicon (100) and corresponding cross sections as found along the *white dotted line*: (a) and (e) 88 mJ/cm^2 pulse fluence having p-polarization at 45° incident angle, (b) and (e) 58 mJ/cm^2 pulse fluence having s-polarization at 0° incident angle, and (c) and (f) 128 mJ/cm^2 pulse fluence having s-polarization at 45° incident angle. The scale bars are 200 nm.

3.8 Plasmonic Laser Nanoablation Threshold for Silicon (100)

For each polarization orientation, we measured the minimum threshold fluence for plasmonic nanoablation. The maximum depth of generated nanocraters for a broad range of laser fluences in measured using AFM and plotted against the average fluence that interacted with the particle at that point. Determination of the relative fluence at the point of particle ablation is nontrivial in those cases where sample irradiance was at an angle. Each nanocrater rests on a distinct plane some distance above or below the beam waist, which can be determined according to its location on the substrate. Since the sample is located at a distance above the Rayleigh range, the spot size interacting at the sample plane will change according to height. Each distinct plane will have a unique spot size that can be found using Eqn 3.2. Determination of the relative fluence at the nanocrater location results from projecting each nanocrater onto its corresponding ablation plane. As shown in Fig. 3.6, a linear fit to data points follows the relationship given in Eqn. 3.4. Extrapolation of the linear fit line to zero provides the "enhanced single-shot ablation threshold". For p-polarized laser light at 45°, the required fluence for surface ablation is reduced to 8.2 ± 2.9 mJ/cm^2. Ablation thresholds determined for laser polarizations parallel to the substrate surface when the substrate is angled 0° and 45°, to the incident irradiation are 27.5 ± 4.3 mJ/cm^2 and 46.7.2 ± 16.3 mJ/cm^2, respectively. The errors were estimated based on the covariance of the data with respect to the linear fit the linear fit. In Eqn 3.4, both α_{eff}^{-1} and $\alpha_{eff}^{-1}\ln\left(F_{abl,th}\right)$ have an associated error. From these errors, we can calculate a set of linear fits that will provide a range of possible ablation thresholds.

The near-field enhancement factor is a measure of the particle's ability to efficiently collect light from a cross-sectional area larger than its geometrical cross-sectional area and scatter it into a nanoscale region necessary for material ablation. Nedyalkov et al. previously determined the near-field enhancement factor by finding the ratio of the laser fluences required to achieve the same ablation depth with and without nanoparticles present on the substrate [13]. We propose the use of the "standard single-shot ablation

threshold" as found from h_a measurements in estimating the nanoparticle near-field enhancement factor. The experimental near-field enhancement factor is estimated using the relationship $\gamma_{eff} = F_{th} / F_{th}^{np}$. For the p-polarized irradiation of a particle at 45° angle, the relationship gives an experimental near-field enhancement of 23.1 ± 7.6. Normal incidence and s-polarized light at 45° give enhancements of 6.9 ± 0.6 and 4.1 ± 1.3, respectively.

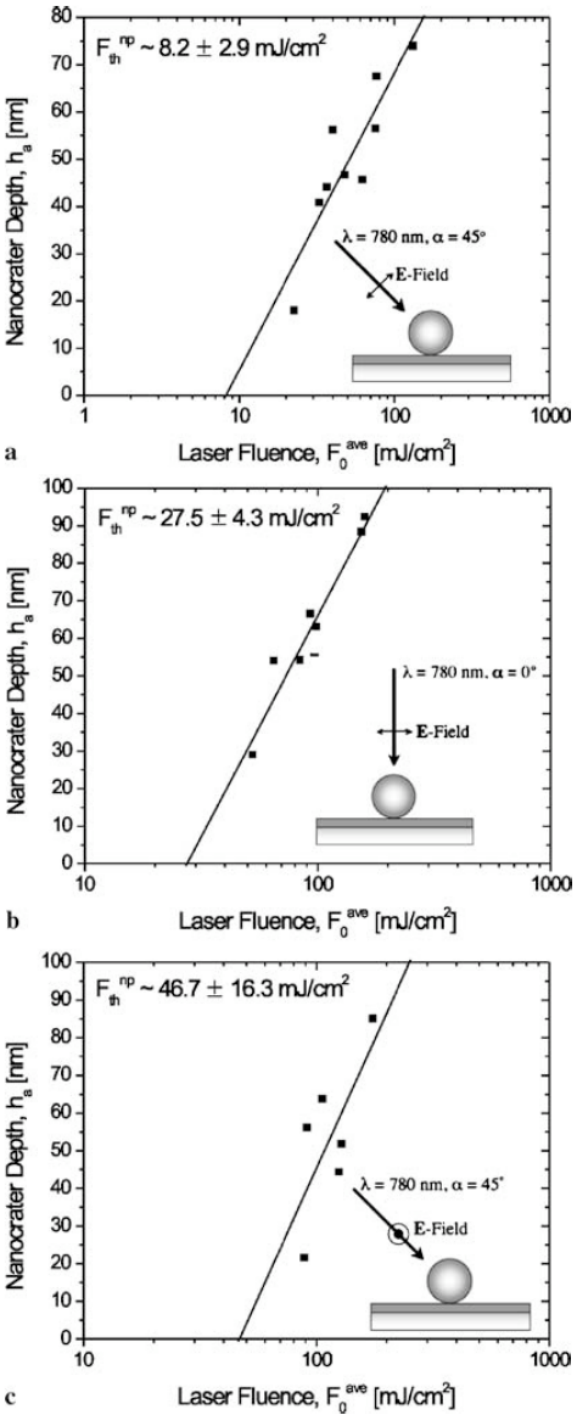

Figure 3.6: Pit depths generated by single 150 nm gold particles are measured at various laser fluences. The depths of the ablation craters are plotted as a function of the laser fluence. Extrapolation of the linear fit to zero provides the enhanced sing-shot ablation threshold. Plots for three different polarizations types were generated: (a) p-polarization at 45° incident angle, (b) normal incidence, and (c) s-polarization at 45° incident angle.

3.9 Comparison to Theoretical Considerations

To validate our measurements, we calculated the near-field intensity based on the solution of the boundary value problem for a spherical particle on a flat semi-infinite substrate [67]. It is assumed that an incident plane wave with a wavelength of 780 nm propagates along the z-coordinate. The angle of irradiation and direction of the electric field are varied according to polarization type. The particle is 150 nm in diameter. Additional multi-reflections between the particle and the substrate, which can lead to further intensity variation along the surface, are taken into account. For a transparent particle on the substrate irradiated with normal incidence, the intensity absorbed by the substrate can be estimated by the following relationship [68]:

$$I \approx \frac{I_0(1-R)}{1-bR}, \tag{3.7}$$

where I_0 is the Mie intensity around the particle when it is not resting on a substrate, R is the substrate reflectivity, and b is the back-scattering efficiency of the particle. When $b < 1$, the intensity will be smaller and for $b > 1$, the intensity will be higher than the Mie intensity. The native oxide layer was ignored because of its negligible effect on the substrate refractive indices. Two sets of calculations were performed to determine the effect of the incident pulse energy absorption by the silicon.

1. Initial experiments are completed with the silicon at room temperature, having optical constants $n = 3.930$ and $\kappa = 0.136$. In this case, the silicon surface does not interact with the incident pulse and the field enhancement around the particle was due solely to the interaction of the laser pulse with the particle. The optical constants of the 150 nm gold particle are calculated using the Drude free electron model, giving $n = 0.195$ and $\kappa = 4.910$ [38].
2. In the second case, we assumed the formation of a low-density plasma along the silicon surface. Here the silicon interacts with the incident pulse by absorbing some of the incident pulse energy. It was assumed that a steady-state plasma was formed at the exact onset of the pulse. Experimentally this will not be the case,

for free electrons will be generated continually over the pulse duration, increasing the surface absorptivity and reflectivity with time. For this general case, optical constants for silicon were given as $n = 4.0$ and $\kappa = 4.5$ [69].

Figure 3.7 shows the calculated field intensity, i.e., the Poynting vector, along the substrate surface for both cases. First, we shall look at the theoretical enhancement for irradiation with *p*-polarized light angled at 45°. We find an enhancement of 17.2 for the first case and 23.9 for the second. This shows that the absorption of the incident energy by the silicon has a large effect on the near-field enhancement of the particle. For simplicity in the calculation, we assumed the formation of a steady-state plasma, but in reality, a plasma with time-dependent density will form during the pulse duration. This agrees with the found experimental results, where the measured field enhancement is between the two theoretical values. As the silicon absorbs the incident energy over the pulse duration, the absorptivity and reflectivity of the silicon will continue to increase, generating larger enhancements in the particle vicinity.

For normal incidence and the *s*-polarization cases, we find larger experimental values than that presented theoretically. A number of factors could be contributing to the increased enhancement. We believe a large part of the extra enhancement contributed to the experimental results for normal incidence is due to increased surface reflectivity, causing a larger number of reflections from the silicon surface to interact with the particle. The reflected waves off the surface will directly interact with the particle. In the *s*-polarized at 45° irradiation case, most of the wave is reflected at an angle away from the particle. Only a small part of the reflected wave interacts with the particle. We see a slight increase in enhancement beyond the theoretically calculated value. Additional factors could include other nonlinear effects due to the ultrashort laser pulses or ultrasmall confinement of light or phase changes in the gold particle during irradiation.

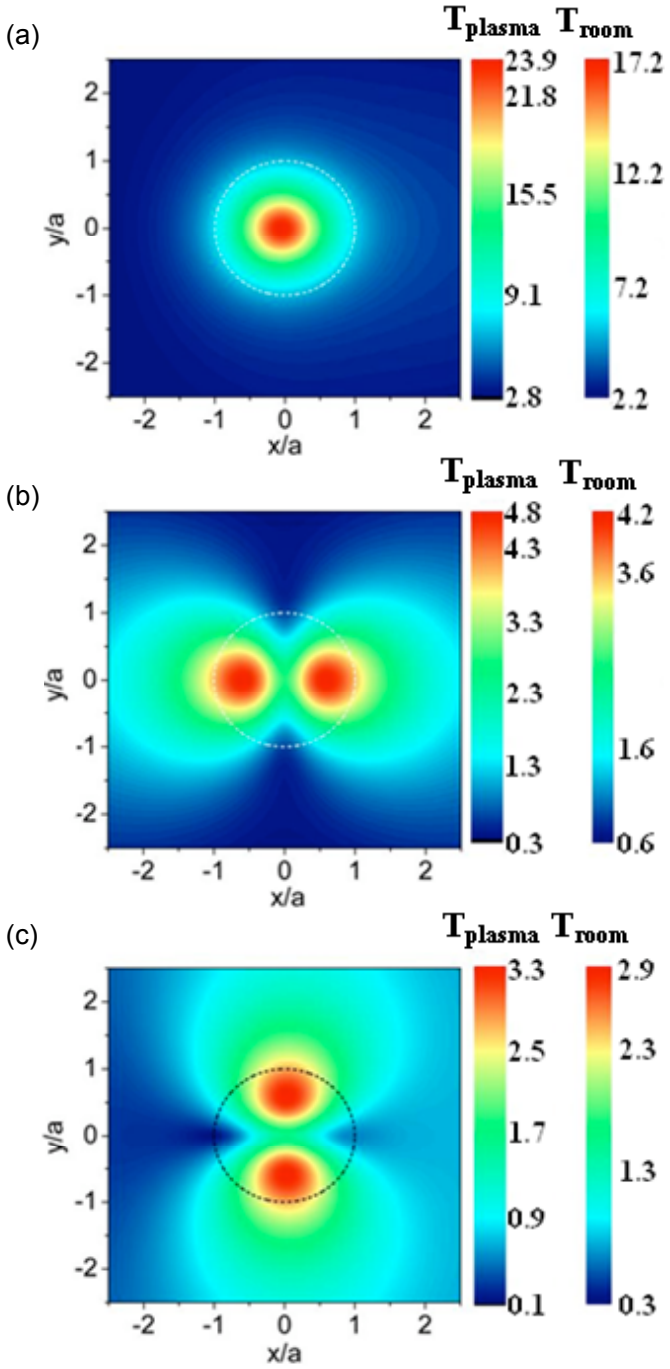

Figure 3.7: Calculated field intensity along the substrate surface, which is based on the solution of the boundary-value problem for a spherical particle on a flat semi-infinite substrate. The 150 nm particle is labeled as the *dotted circle*. T_{plasma} and T_{room} describe the field enhancement with and without the addition of the low-density plasma generated along the silicon surface, respectively. (a) p-polarization at 45° incident angle, (b) normal incidence, and (c) s-polarization at 45° incident angle.

3.10 Concluding Remarks

We demonstrated the nanoscale ablation of silicon (100) using the plasmonic enhancement of femtosecond laser pulses in the near-field of spherical gold particles. The influence of laser polarization and angle of ablation on generated craters were investigated and characterized by AFM and SEM. It was found that there is a linear relationship between crater depth and the logarithm of the average laser fluence. Extrapolation of the linear relationship to zero provides the enhanced single-shot ablation threshold. Results show that particles irradiated with *p*-polarized light have the greatest enhancement, reducing the required fluence for silicon ablation by 23.1 ± 7.6 times. Normal incident light reduced the ablation threshold by 6.9 ± 0.6 times, while *s*-polarized light at 45° had a 4.1 ± 1.3 times reduction. Measured crater morphologies, as predicted in our theoretical calculations, were direct imprints of the dipolar scattering region around the particle. The measured near-field enhancement values agree well with the maximum field enhancements obtained in our calculations. Agreement between theory and measurements supports that the nanocraters were indeed formed by the enhanced plasmonic scattering in the near-field of the nanoparticles. The formation of a low-density plasma on the surface due to the incident laser pulse was found to increase the particle enhancement at the substrate surface.

Chapter 4: Plasmonic Laser Nanoablation of Borosilicate Glass

Borosilicate glass is a dielectric material that exhibits similar femtosecond laser ablation properties as that of biological materials, making it a model substrate to study the plasmonic ablation of tissue in a controlled environment. We studded a borosilicate glass surface with a broad distribution of particle arrangements ranging from single 80 nm particles to micron-sized aggregates. Three effects were studied: (1) minimum threshold fluence necessary for plasmonic nanoablation in the single- and multi-particle cases; (2) effect of cluster orientation with respect to laser polarization on minimum threshold and crater morphology; (3) effect of cluster size and geometry on minimum threshold.

4.1 Experimental Approach

The experimental setup utilized in the glass experiments was the same as that in the silicon experiments and the reader can refer to Fig. 3.1 for a sketch of the experimental setup. To be noted, before the experimental set was performed, the setup was relocated closer to the laser cavity, which modifies the irradiation spot size due to a change in the beam quality. In plasmonic ablation experiments, the sample was placed 60 μm from the beam waist to obtain a larger spot size. As is shown in Fig. 4.1, at the irradiation plane, an elliptically shaped spot having a measured $1/e^2$ short axis radius of $w_{0x} = 6.6 \pm 0.3$ μm and a long axis of $w_{0y} = 7.0 \pm 0.2$ μm was found using Eqn. 3.1 [61]. Uncertainty in the ablation threshold measurement arises mainly due to the error in the measured spot size and pulse-to-pulse energy variability of 5%.

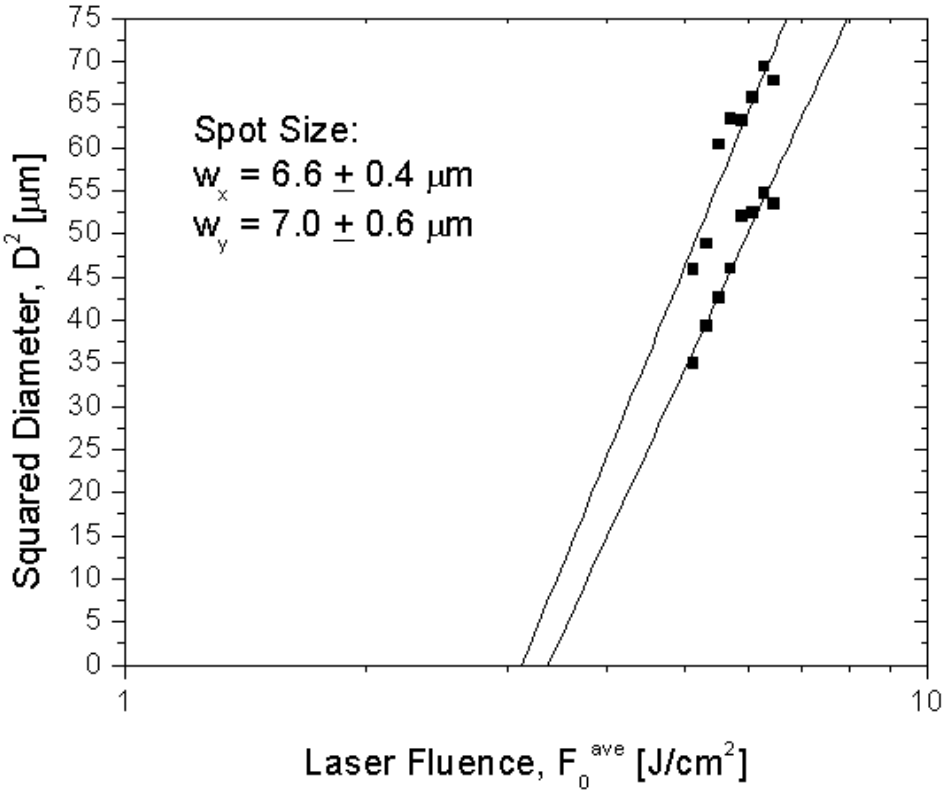

Figure 4.1: The squared diameter of the laser-induced damage on the borosilicate glass is plotted as a function of the laser fluence. The slope of the linear fit provides the $1/e^2$ Gaussian beam waist at the plane of ablation. The ablation region was measured using AFM.

A 1.1 mm thick borosilicate glass plate (Borofloat, < 1 nm surface roughness; Precision Glass and Optics, Santa Ana, CA) was cut into 5 x 5 mm pieces and washed in methanol under sonication for 25 minutes. The chemical composition of borosilicate glass is 81% SiO2, 13% B2O2, 2% Al2O3, and 4% NaO2 and its band gap energy is about $E_b \sim 4$ eV [70].

80 nm gold particles were produced according to the Turkevich method, in which particles were synthesized by the reduction of $HAuCl_4$ with sodium citrate [71,72]. This method provides precise size control; produced spherical particles had a size distribution of 4% (characterized using SEM and AFM). Additionally, a monodisperse colloidal suspension remains due to citrate ions coating particle surfaces.

A 6 microliter aliquot of colloidal gold was deposited onto the surface and the sample was annealed in air at 120 °C for five minutes. By slowly heating the surface, we were able to obtain a broad distribution of particle arrangements on the surface ranging from single particles to micron-sized aggregates.

Samples were characterized before and after irradiation using AFM (Dimension 3100; Digital Instruments). The AFM was operated in tapping mode in air using triangular shaped silicon cantilevers (40.0 N/m spring constant and 300 kHz resonance frequency; Budget Sensors).

4.2 Femtosecond Laser Ablation of Dielectric Materials

Transparent materials do not absorb radiation from the visible to near-infrared portions of the electromagnetic spectrum. As is such, optical breakdown in transparent materials requires incident fields of high peak intensities. Femtosecond laser pulses can, however, provide high peak intensities exceeding 10^{11} W/cm^2 necessary to initiate nonlinear absorption processes of the incident laser energy. Large numbers of electrons in the medium are excited by the high flux of photons, since the electrostatic force felt by the valence electrons becomes large enough to excite the bound electrons out of the Coulomb potential [73]. A sufficiently high electron density plasma results. Plasma electrons continue to gain energy via the laser field and impact collisions with neighboring atoms. When the density of free conduction band electrons reaches a critical density, optical breakdown occurs and no further energy from the laser field is deposited. After the pulse has passed, electrons and ions equilibrate and the plasma expands, ejecting material from the irradiated region. The minimum fluence necessary to initiate ablation is called the optical breakdown threshold and materials experience permanent modification [74].

Since femtosecond pulses are of high intensity, optical breakdown is intrinsically different from that of longer pulse ablation. During femtosecond laser ablation, seed free electrons are generated through nonlinear absorption processes independent of the initial electron concentration in the material. In contrary, when ablating materials with pulses

greater than 10 ps, material impurities provide the source for seed electrons [75]. Also, since the pulse duration is shorter than the material heat conduction time, laser energy is absorbed by electrons only and a high density plasma is generated before substantial heat diffusion to the surrounding lattice occurs. Thus there is no change in the electron-lattice dynamics during the laser absorption process [76]. The intense heating and rapid expansion of material at the focal volume are the only factors that account for the vaporization of the bulk material.

We found the single-shot ablation threshold of borosilicate glass in air to be $F_{abl,th}$ = 1.88 ± 0.05 J/cm^2, which agrees well with literature [62,77,78]. This threshold was determined from the data presented in Fig. 4.2, where the linear fit, as determined by Eqn 3.4, was extrapolated to zero.

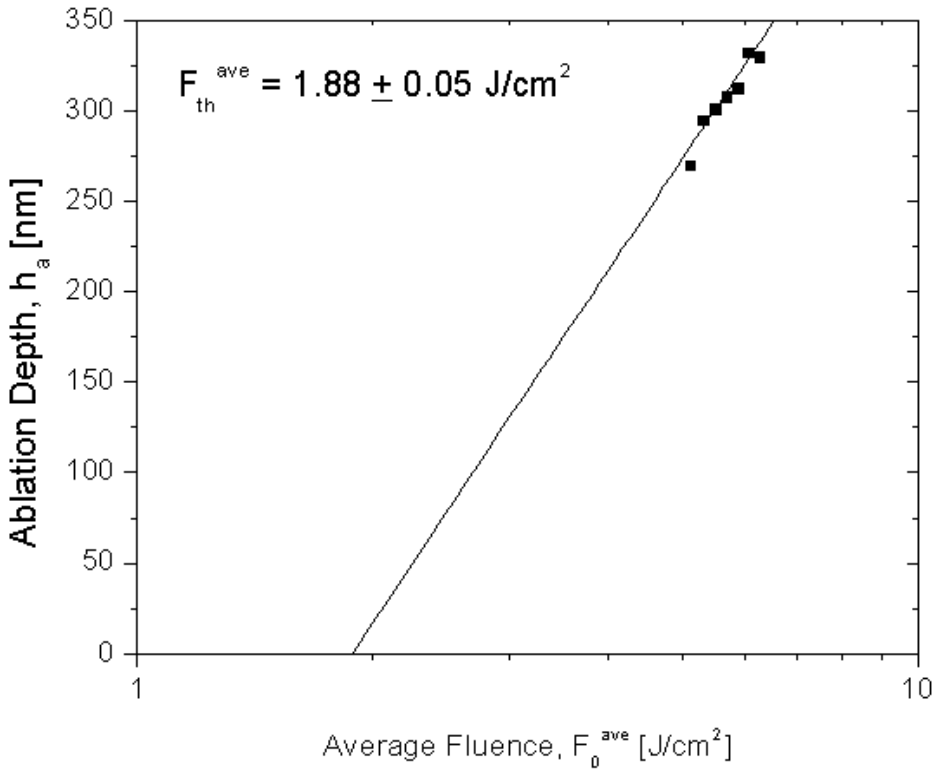

Figure 4.2: The depth of the laser ablated borosilicate glass crater is plotted as a function of the laser fluence. Extrapolation of the linear fit to zero provides the single-shot femtosecond laser ablation threshold of borosilicate glass.

4.3 Plasmonic Laser Nanoablation by Single Particles

Figure 4.3 shows a crater generated by a single particle irradiated with normally incident light having a relative fluence of 1.2 J/cm^2. The crater has a double-lobed structure, which follows the dipolar scattering pattern of the nanoparticle. Crater dimensions are approximately 30 nm depth and 270 nm width at the surface. No residual gold was found in the crater vicinity. Since the femtosecond laser ablation threshold of dielectrics is approximately an order of magnitude higher than that of gold, the gold nanoparticle will ablate at each nanoablation site. The gold nanoparticle ablation threshold of 20 to 25 mJ/cm^2, which we define as the laser fluence below which the whole spherical structure of the particle remains intact, was again verified in the glass experiments.

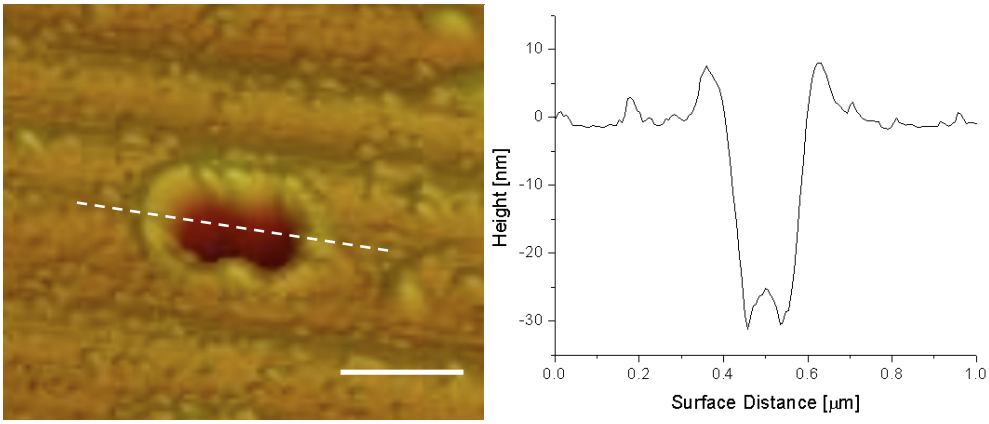

Figure 4.3: (a) AFM images of nanocraters ablated by 80 nm gold nanoparticles on borosilicate glass and (b) corresponding cross section as found along the *white dotted line*: 1.2 J/cm^2 pulse fluence at normal incidence. The scale bar is 200 nm.

To determine the minimum threshold necessary for plasmonic nanoablation, the maximum depth of generated nanocraters is measured using atomic force microscopy and plotted against the relative fluence that interacted with the particle at that point. As shown in Fig. 4.4, a linear fit to data points follows the relationship given in Eqn. 3.4. Extrapolation of the linear fit line to zero provides the "enhanced single-shot ablation

threshold". Using this technique, we find a single particle threshold fluence of 227 ± 38 mJ/cm^2, which correlates to an optical enhancement of 8.3 ± 1.2.

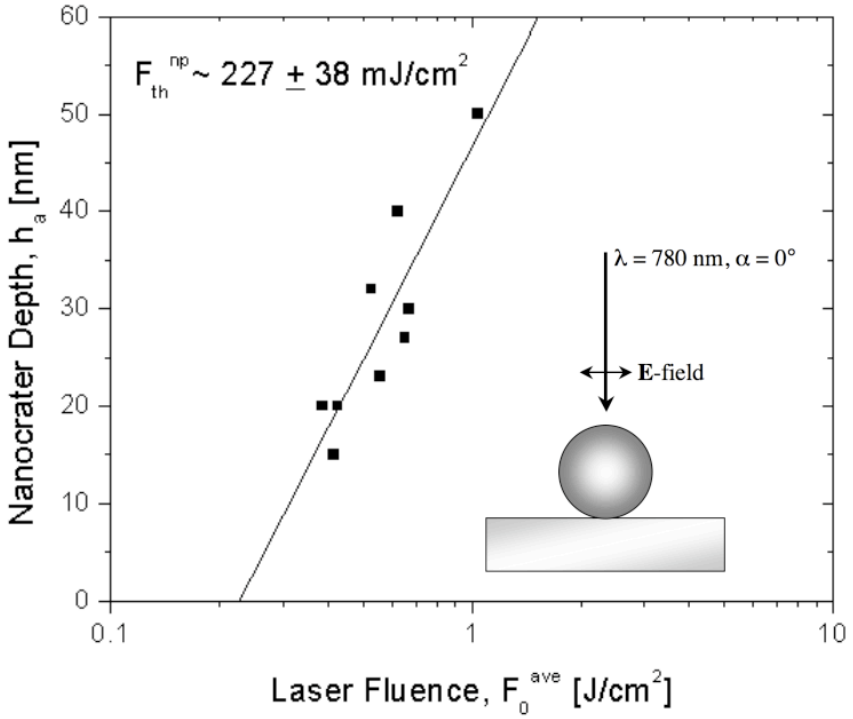

Figure 4.4: Pit depths generated by single 80 nm gold particles are measured at various laser fluences. The depths of the ablation craters are plotted as a function of the laser fluence. Extrapolation of the linear fit to zero provides the enhanced sing-shot ablation threshold. Craters were generated with irradiation at normal incidence.

Using the same model as presented in the silicon data, we found the theoretical enhancement of an 80 nm, gold nanosphere resting on a semi-infinite dielectric substrate irradiated by 780 nm laser light [67]. The simulation was run without the formation of a low-density plasma during irradiation. Figure 4.5 shows the calculated field intensity, i.e., the Poynting vector, along the substrate surface. We find an enhancement of 1.67. This value, as in silicon experiments, is lower than the found experimental enhancement. Again, it is reasonable to assume the formation of a time-dependent low-density plasma during irradiation would increase the degree of enhancement.

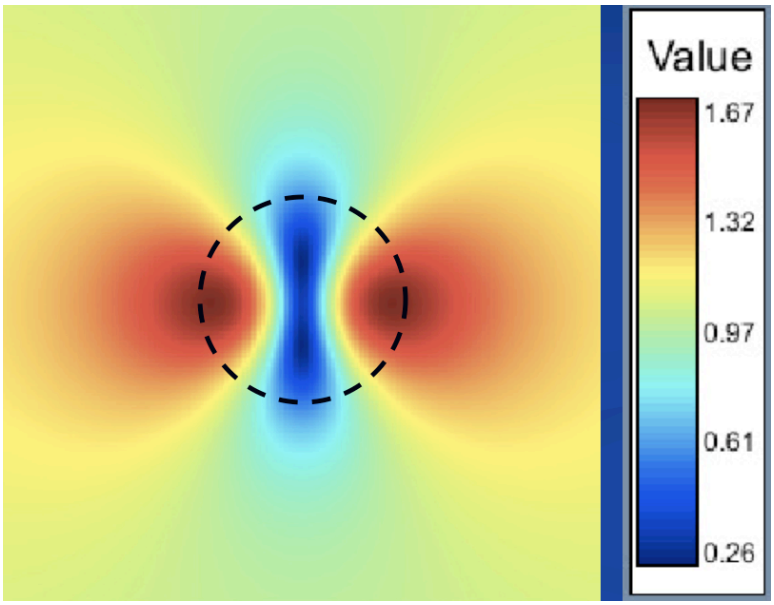

Figure 4.5: Calculated field intensity along the substrate surface, which is based on the solution of the boundary-value problem for a spherical particle in air on a flat semi-infinite substrate. The 80 nm particle is labeled as the *dotted circle*. The low-density plasma typically generated along the silicon surface was not included in calculation. Irradiation was at normal incidence.

4.4 Plasmonic Laser Nanoablation by Particle Aggregates

Randomly oriented particle aggregates exhibit ablation dynamics significantly more complicated than that of single particles. The near-field enhancement factor is now a function of all of the scattered waves from individual particles and electromagnetic particle couplets within the aggregate. Electromagnetic particle couplets can consist of two or more electromagnetically coupled particles depending upon the incident irradiation. Traditionally, the aggregate near-field enhancement is given mathematically by through the superposition of scattered waves from indiviual particles [60]:

$$Q_{NF}(N) = \frac{Q_{sca}(N)}{N \cdot Q_{sca}(1)} \tag{4.1}$$

where N is the aggregate size and

$$Q_{sca}(N) = \frac{2}{(ka)^2}\sum_{i=1}^{N}\sum_{n=1}^{\infty}\sum_{m=-n}^{n}\left|\alpha_{nm}(i)\right|^2 + \left|\beta_{nm}(i)\right|^2 + \frac{2}{(ka)^2}\sum_{i=1}^{N}\sum_{n=1}^{\infty}\sum_{m=-n}^{n}\mathrm{Re}\left\{\alpha_{nm}^{*}(i)\left(1-\frac{\alpha_{nm}(i)}{\alpha_{n}(i)}\right)+\beta_{nm}^{*}(i)\left(1-\frac{\beta_{nm}(i)}{\beta_{n}(i)}\right)\right\} \tag{4.2}$$

Essentially, primary particles in the aggregate electromagnetically couple, exhibiting additional extinction features at longer wavelengths λ, where the surface plasmon is strongly decreased in single particle irradiation. We propose that primary particles can be composed of an assortment of electromagnetic particle couplets ranging from single particles to larger aggregate sizes. Electromagnetic couplet formation is defined through the direction of the incident electric field and orientation of particles within the aggregate, which can vary the number and size of the resulting couplets. Effectively, the dominant source of the near-field enhancement generation changes with aggregate size. For, example, small clusters will have near-field enhancements dominated by electromagnetic particle cuplets. Of additional importance to plasmonic laser nanoablation is the fact, at longer wavelengths, the plasmon band is dominated by scattering processes; absorption still dominates in shorter wavelengths, but will again be negligible in the near-infrared regime.

4.4.1 Crater Morphology and Plasmonic Laser Nanoablation Threshold

Crater morphology and the single shot ablation threshold depend upon aggregate size, geometry, and orientation to the laser polarization. Since much of the scattered waves are confined within an aggregate, generated craters are generally direct imprints of the aggregate size and geometry. Crater profiles exhibit nanoarchitecture describing the location of the individual particles in the cluster. As with single particles, it is again feasible to elucidate the aggregate ablation threshold via the linear relationship between the single-shot ablation depth and the logarithm of the relative laser fluence. However, the relationship is only valid when comparing craters generated by particle aggregates of the same number of particles and geometry, in addition to the same orientation to the

laser polarization.

The minimum fluence necessary for ablation by two- and three-particle aggregates oriented at a 45° angle to the laser polarization has been studied. Individual particles within each aggregate system were in direct contact. The two-particle aggregate ablation threshold is 132 ± 22 mJ/cm^2, yielding a near-field enhancement of 12.2 ± 2. We find a threshold of 52 ± 9 mJ/cm^2 for the three-particle aggregate, yielding a near-field enhancement of 28.8 ± 4.8. Figure 4.6 compares the ablation threshold values for the single-, two-, and three- particle aggregate cases two particle, and three particle clusters. As is evident, the ablation threshold decreases with an increasing number of particles found within an aggregate. The increased enhancement is a direct result of the constructive interference of all the individually scattered fields within the cluster. This generates "hotspots," regions of strong scattered wave interaction, of which the location depends upon the aggregate orientation to the laser polarization.

As was mentioned, enhanced single-shot ablation threshold relationship is only valid for particle aggregates having the same geometry and orientation with respect to the laser polarization. To experimentally verify this, lets provide a brief experimental example. We make the statement that the ablation process is highly dependant on the laser polarization direction. If we observe two independent three particle clusters irradiated with a relative fluence of 470 mJ/cm^2. One cluster is oriented in the direction of the polarization and the other is at a 45° angle to the laser polarization. The cluster positioned along the polarization direction has a depth of 10.3 nm, while the other cluster has a depth of 2.5 nm. It can be concluded that the cluster positioned along the direction of polarization will have a greater enhancement, leading to a lower ablation threshold value. Theoretically, this particle coupling can be described using the dipole-dipole interaction model [79].

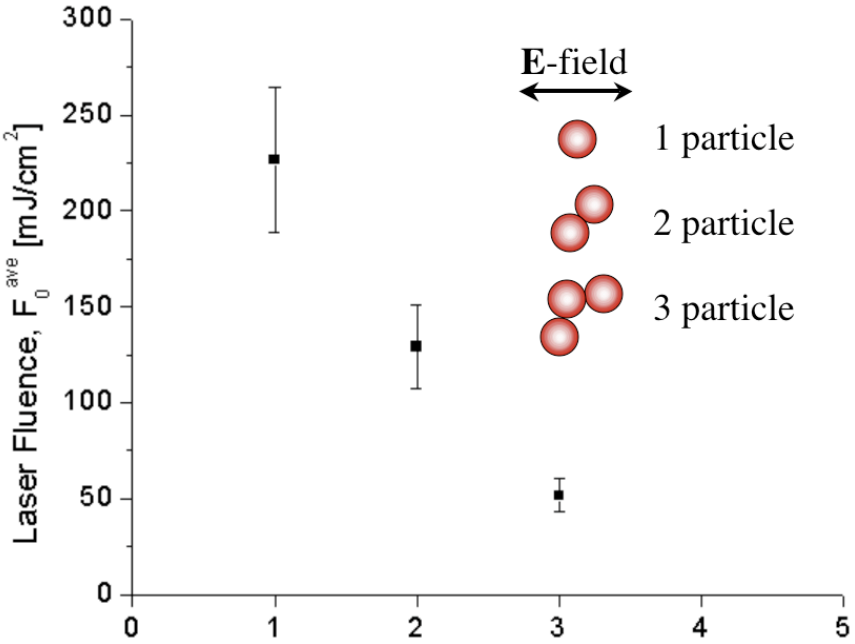

Figure 4.6: Aggregates of one-, two-, and three-particles oriented at a 45° to the incident electric field were studied. Their corresponding enhanced ablation threshold were plotted to show the threshold fluence dependency on aggregate size.

4.4.2 Dipole-Dipole Interaction Model

Theoretically, we can describe the formation of electromagnetic couplets within an aggregate using the dipole-dipole interaction model. As described in detail in chapter 2, surface plasmons are confined along the particle surface. When certain resonant conditions are met, the system becomes resonant and the particle strongly interacts with the incident light. Lets place a second particle within the near-field of the first particle. Upon polarization of the conduction electrons by the incident field, additional forces act upon both particles. First, lets observe a particle pair oriented such that the long axis is orthogonal to the incident electric field. In this case, the repulsive force of the surface charges is enhanced, leading to a higher resonance frequency and effectively blue shifting the plasmon resonance. Here we will find a lesser degree of near-field scattering at higher wavelengths and a reduced near-field enhancement factor. The opposite effect occurs when the electric field is parallel to the long axis of the particle pair. In this case, the plasmon band shifts and stronger enhancement will be seen in the near-infrared.

Figure 4.7 provides a schematic of the dipole-dipole model. Figure 4.8 provides experimental evidence for the particle coupling effect for two 150 nm diameter particles having 17 nm height. Through the dipole-dipole model, we can observe how electromagnetic particle couplets provide strong near-field enhancement at the 780 nm wavelength.

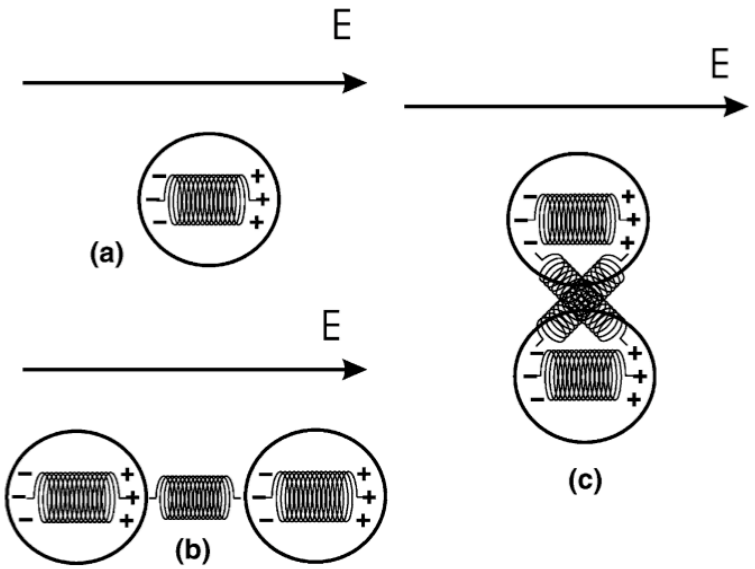

Figure 4.7: Schematic demonstrating the electromagnetic coupling of two closely spaced nanoparticles based on the dipole-dipole interaction model. (a) isolated particle, (b) particle pair with electric field parallel to particle-pair long axis, and (c) particle pair with electric field perpendicular to particle-pair long axis. Reproduced from [80].

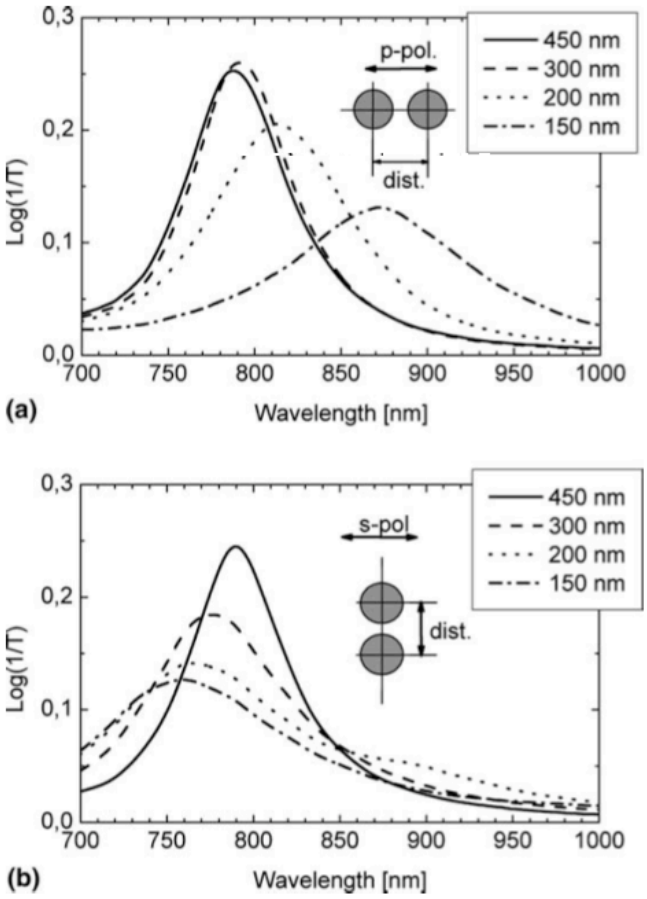

Figure 4.8: Experimental result of the extinction spectra for a 2D array of gold nanosphere particle-pairs with varying interparticle center-to-center distances. Orthogonal particle separation is kept constant. Each curve represents a single interparticle center-to-center distance as shown in the upper-right hand corner. Polarization direction is (a) parallel to particle-pair long axis and (b) perpendicular to particle-pair long axis. Reproduced from [80].

4.4.3 Limitations of Particle Aggregation

Since aggregates generate large enhancements via scattered wave interactions from both individual particles and electromagnetic particle couplets, two phenomena will limit the functionality of aggregate ablation: (1) particle "cross-talk" and (2) destructive interference. Aggregate size has a finite limit, beyond which the maximal optical enhancement saturates. As more particles are added to the aggregate, particles along the aggregate edge are moved to greater distances from aggregate center. In general, with

increasing interparticle distance, the amplitude of the interfering scattered waves decreases. At some saturation point, no additional enhancement from cross-talk by the outer most particles in the aggregate occurs. The saturation point is determined by the orientation of the particles within the cluster. For example, aggregates forming a rod shape of single particles will saturate with less particles than that of spherically shaped aggregates. Currently, the particle distance at which the saturation point occurs has not been determined. It is conjectured from our present data, that this saturation point will occur approximately at interparticle distances of approximately 5-7 particles. Theoretically, Quinten finds that near-field intensities drop off to far-field values at R = 5a, which compares well with our experimental prediction [60].

Randomly oriented clusters will be limited in size by deconstructive interference of the scattered waves. Each individual emitter in an aggregate, whether a single particle or electromagnetic particle couplet, scatters light with a particular angular orientation and phase [60]. Additionally, the degree of enhancement from electromagnetic particle couplets within an aggregate will affect the degree of enhancement depending upon the coupling orientation [80]. Together, these two physical electrodynamic properties will result in light of different phase to interact and effectively reduce the overall enhancement. Generally, we find deconstructive interference to affect randomly oriented cluster of 10 particles or more. It is through the described limitations of aggregate ablation that we theorize that the aggregate near-field enhancement factor is the superposition of all of the scattered waves from individual particles and electromagnetic particle couplets within the aggregate.

4.5 Concluding Remarks

We demonstrated the nanoscale ablation of borosilicate glass using the plasmonic enhancement of femtosecond laser pulses in the near-field of spherical gold particles. The influence of particle aggregation on generated craters was investigated and characterized by AFM. It was found that there is a linear relationship between crater depth and the logarithm of the average laser fluence only for craters generated by clusters

of the same geometry, size, and orientation to the laser polarization. Extrapolation of the linear relationship to zero provides the enhanced single-shot ablation threshold. Results show that in general, aggregate size increases the degree of near-field enhancement via electromagnetic coupling of the individual particles within the aggregate. Single particle ablation had an enhancement of 8.3 ± 1.2, while two- and three-particle clusters oriented at a 45° to the incident electric field had near-field enhancements of 12.2 ± 0.2 and 28.8 ± 4.8, respectively. The degree at which aggregate size heightens the near-field enhancement was found to be limited by particle cross-talk and deconstructive interference. Measured crater morphologies, as predicted in our theoretical calculations, were direct imprints of the dipolar scattering region around the particle. The measured near-field enhancement values agree well with the maximum field enhancements obtained in our calculations. Agreement between theory and measurements supports that the nanocraters were indeed formed by the enhanced plasmonic scattering in the near-field of the nanoparticles. The formation of a low-density plasma on the surface due to the incident laser pulse was found to increase the particle enhancement at the substrate surface.

Chapter 5: Conclusion and Outlook

The results presented in this thesis are only the first steps toward the near-field optical processing of solid materials. We have demonstrated the nanoablation of both semiconductor and dielectric materials by the enhanced plasmonic scattering of 780 nm, 220 fs laser pulses in the near-field of gold nanospheres. Experimentally we studied the effect of polarization and particle aggregation on crater morphology and near-field enhancement. Listed below is a summarization of found results:

1. On both substrates, generated nanocrater morphologies show a direct imprint of the particle dipolar scattering region.
2. The largest near-field enhancements for single particle ablation were found when the incident radiation was directed at a 45° angle into the substrate surface. The near-field enhancement was found from the ratio of the standard single-shot ablation threshold with and without nanoparticles present on the substrate surface.
3. Ablation by particle aggregates had a greater efficiency than that by single particles due to the electromagnetic coupling of individual particles in the aggregate. The degree of near-field enhancement depends upon the aggregate geometry, size, and orientation with respect to the laser polarization.
4. The formation of a time-dependent, low-density plasma along the substrate surfaces during laser irradiation greatly enhanced the efficiency of the process. The absorptivity and reflectivity of the substrate surface was heightened via low-density plasma formation, allowing for greater light interaction between the nanoparticle and substrate.

5.1 Future Project Outlook

Future goals for the technological use of plasmonic laser nanoablation include the development of a subcellular nanosurgery technique and nanolithographic technique. For

these technologies to become reality, a few basic phenomena need more experimental understanding: (1) the effect of particle composition and geometry, (2) the effect of interparticle distances in randomly oriented aggregates, (3) electromagnetic energy transport in ordered particle matrices, and (4) the role of the low-density plasma.

5.1.1 Particle Shape and Material Composition

The spectrum of the near-field efficiency for a noble-metal nanoparticle is dependent upon the particle's material composition and geometry [23]. By changing the two aforementioned material properties, it is plausible to obtain a wide range of enhancement wavelengths and plasmon polariton magnitudes.

Changing the nanoparticle material composition is the most trivial of the solutions. Localized surface plasmons resulting in strong near-field scattering occurs in particles made from all noble-metal types. As such, particles can be composed of any of the noble-metals or from composites of two or more noble-metals [81-82]. For example, switching from a gold nanosphere of diameter $2a = 44$ nm to a silver particle of the same dimension affords an increase in the peak near-field enhancement of 15 times [59]. Such a material composition switch works well with nanolithographic techniques, but biocompatibility limitations will exist in biological applications. In general, it is agreed that gold is the most biocompatible of the noble-metals. To circumvent this biocompatibility issue, one method of achieving larger enhancements is via a metal-metal heterosystem [81]. As an example, a silver nanoparticle can be coated with a layer of gold. Other suitable nanoparticle types include carbon nanotubes or other carbon-based nanostructures [83]. However, at this point, the biocompatibility of carbon-based structures is unknown.

The fundamental spherical particle shape, with which all experiments were performed in this thesis, generally has the lowest overall enhancement [84]. Sharp edges [85] or surface irregularities [86] on the particle surface increase the overall enhancement; especially large local enhancements can be found at sharp edges. By adjusting the particle geometry, is feasible to generate large near-field scattering

enhancements at wavelengths far from the absorption resonance. For example, Krug II *et al*. showed that right trigonal pyramids composed of gold and having a 45° cone angle and 675 nm long conical tip illuminated by a 825 nm wavelength plane wave can theoretically generate intensity enhancements of order 7400 [87]. Additionally, they showed that even the simple gold spheroid can generate enhancements of order 1600 depending on the major- and semimajor-axis lengths [87]. Gold can be fashioned into a variety of other particle geometries such as rods [88], triangles [89], and nanorice [90].

Experimentally testing the ablation threshold as a function of geometry and material compositions can be performed in a similar manner to that presented in this thesis. Deposition of the particles can be either be through growth of the nanostructures directly onto the substrate by e-beam lithography or other modified lithographic techniques or particles can be wet deposited onto the surface as was done in this thesis. With different particle geometries, orientation of the incident electric to the deposited particles becomes of great importance [87]. Through the interaction of the major- or semimajor particle axis with the incident field, separate resonant fields can be excited. To determine the peak obtainable optical enhancement of the particle type, knowledge of the particle orientation before irradiation will be of the upmost importance. It is the author's opinion that sharp-tipped particle shapes will have the most impact on nanosurgery techniques while spherical particle composed of a highly scattering material will become most important to nanolithographic techniques.

5.1.2 Interparticle Distances in Randomly Oriented Aggregates

It has been experimentally determined that particle aggregates greatly increase the degree of near-field enhancement. The scattering angle, phase of scattered light, and electromagnetic coupling of particle pairs are dependent upon the direction of the incident electric field. This leads to particle cross-talk and interference, limiting the maximal functional aggregate geometry and size.

Particle aggregation has been shown to be a critical facet of cellular ablation [91,92]. In our lab, the next step is the development of a plasmonic laser nanosurgery

technique for the specific removal of dysplastic cells. Sokolov *et al*. recently demonstrated a new class of contrast agents having a high affinity for cellular biomarkers [93]. Specifically, they conjugated gold nanoparticles with monoclonal antibodies against the epidermal growth factor receptor (EGFR). This provides a highly specific nanoparticle delivery method to epithelial cancer cells. Upon irradiation of the nanoparticle bound cells by a low fluence, large spot size, femtosecond laser pulse, plasma-mediated ablation of the membrane by near-field scattering will occur. It has been shown in photothermal laser therapy, with the application of low laser fluences, unlabeled cells will remain intact whilst labeled cells will die through necrotic processes [91]. Since EGFR is unevenly dispersed across the cell membrane, gold nanoparticle aggregates will form during labeling. The degree of aggregation depends upon the nanoparticle load per cell. If the membranes are overloaded with nanoparticles and large clusters form, the clusters may no longer contribute to the overall ablation enhancement. This in turn could require the physician to irradiate cellular structures with greater amounts of energy, possibly damaging healthy cells in the vicinity of the desired ablation zone. It will be of the upmost importance to study the aggregation of nanoparticles on the cellular membrane as a function of particle loading.

In addition to live studies, it will be fundamental to further study particle aggregation in a controlled environment. We propose the use of a molecular ruler to study the affect of interparticle distances within randomly oriented aggregates. ss-DNA can be used as a nanometer ruler by varying its length through the addition of adenine bases [94]. Individual 80 nm gold nanospheres will be coated with thiolated ss-DNA molecular rulers, which can be covalently attached to the nanoparticle surface via the thiol moiety. To attach the thiol moiety to the 5' end of the polyadenine chain, a six carbon methylene spacer needs to be first attached. The coated nanoparticles will then be deposited onto a bare borosilicate glass surface. Through the variation of the ss-DNA strand length, we can vary the interparticle distance in nanoparticle aggregates and study the ablation dynamics.

Since nanospheres will be coated with αEGFR in a biological setting, we propose to study the ablation parameters of αEGFR conjugated nanospheres deposited onto a borosilicate glass surface. Through this experiment, a few biological properties can be modeled in the experiment:

1. A broad distribution of particle arrangements ranging from single bioconjugates to micron-sized bioconjugate aggregations will be found along the surface.
2. The dielectric interface will simulate the biological membrane.
3. Since the nanoparticles are antibody coated, they will not sit directly upon the interface surface.
4. Surface antibodies will separate closely spaced interacting particles, which will also be true in biological models.

Such a system will provide a test bench to understand the ablation properties of gold bioconjugates in a controlled manner. In each of the experimental cases listed above, the enhanced single shot threshold technique used in the prior silicon and glass experiments will again be valid, providing a simple technique to study ablation parameters for biological systems in an "*in vitro*" setting.

5.1.3 Ordered-Particle Matrices

In contrast to many biological applications, regularly ordered-particle matrices will be extremely important to the fields of nanolithography, nanomachining, and optical "ink-jet" printing methods. Just recently, there was a huge jump in the field of lithographic printing; Kraus *et al*. successfully developed a high throughput nanoparticle printing process with single-particle resolution [95]. This opens up the door, so to speak, for the introduction of plasmonic laser nanoablation to optical printing technologies. Difficulty here lies in the ability to space particles close enough, such that they cross-talk and generate lines between them during the ablation process. Additionally, for the ablated channels to be of use, the channel profile must be relatively smooth and free of height variations. This would require a great deal of electromagnetic energy transport studies to

performed on ordered particle matrices as the single-nanoparticle technology continues to develop. Quinten *et al*. theoretically studied laser energy transmission loss along particle chains and found the minimum loss to equal a center-to-center distance to particle radius ratio of approximately 3 [96]. For 80 nm gold spheres, that would require particles to be separated by center-to-center distances of 120 nm, which is still below the current resolution of the system.

At this point, one possible experiment for the understanding of ordered matrices, would be to study the interaction of ordered gold triangles on a silicon surface. Burmeister et al. developed a simple technique to generate highly ordered arrays of gold triangles using a monolayer of monodisperse spherical particles servicing as a deposition mask [97,98]. Here, it is possible to position triangles close enough for electromagnetic coupling to occur. With the triangular shape, we can experimentally "choose" which triangle tips we would like to cross-talk by varying the direction of the electric field incident the surface. Through the use of AFM and SEM, ablated lines between the triangle tips can be fully characterized.

5.1.4 Low-Density Plasma Formation

Our experimental studies have revealed that the formation of a low-density plasma during laser irradiation greatly increases the overall near-field enhancement. It is still unknown what the coupling strength of the low-density plasma is to the nanoparticle. We again propose the use of the molecular ruler ss-DNA to elucidate the coupling strength. The distance of the particle to the substrate surface can be varied through the attachment of ss-DNA to the surface of a borosilicate glass substrate. Bare 80 nm gold nanospheres will be deposited onto the coated interface. At each particle/surface separation distance, the relative near-field enhancement can be determined; with increasing distance, we expect the relative near-field enhancement to decrease to no ablation has occurred.

5.2 Summary

In this thesis, we presented experimental evidence for the near-field optical processing of solid materials via the plasmonic scattering of near-infrared laser light. A few of the basic ablation principles were studied on two different material substrates. With scientific exploration always comes the continuous line of questions. A few of these basic phenomenon that still need to be studied were presented with some example experiments that may elucidate their sought answers. Future goals for the technological use of plasmonic laser nanoablation in our lab include the development of a subcellular nanosurgery technique and nanolithographic technique. With the continued development of the project, this near-field scattering technique may become gold standard in a great number of fronts such as cancer therapy, nanomachining, nanolithography, cardiology, brain surgery, Mohs surgery, burn victim treatment, optical computing, and optical inkjet printing.

References

1. A.A. Gorbunov, W. Pompe, Phys. Status Solid. A **145**, 333 (1994)
2. J. Jearsch, F. Demming, L.J. Hildenhagen, K. Dickmann, Appl. Phys. A **66**, 29 (1997)
3. K. Wilder, C.F. Quate, D. Adderton, R. Bernstein, V. Elings, Appl. Phys. Lett. **77**, 2527 (1998)
4. A. Chimmalgi, C.P. Grigoropoulos, K. Komvopoulos, J. Appl. Phys. **97**, 104319 (2005)
5. S. Nolte, B.N. Chichkov, H. Welling, Y. Shani, K. Lieberman, H. Terkel, Opt. Lett. **24**, 914 (1999)
6. L. Wang, E.X. Jin, S.M. Uppuluri, X. Xu, Opt. Exp. **14**, 9902 (2006)
7. D.J. Hwang, A. Chimmalgi, C.P. Grigoropoulos, J. Appl. Phys. **99**, 044905 (2006)
8. W. Srituravanich, N. Fang, C. Sun, Q. Luo, X. Zhang, Nano Lett. **4**, 1085 (2004)
9. S.M. Huang, M.H. Hong, B. Luk'yanchuk, T.C. Chong, Appl. Phys. A **77**, 293 (2003)
10. W. Cai, R. Piestun, Appl. Phys. Lett. **88**, 111112 (2006)
11. A.J. Heltzel, A. Battula, J.R. Howell, and S.C. Chen, J. Heat Transf. **129**: p. 53 (2007).
12. S.M. Huang, M.H. Hong, B. Luk'yanchuk, T.C. Chong, Appl. Phys. Lett. **82**, 4809 (2003)
13. N.N. Nedyalkov, H. Takada, M. Obara, Appl. Phys. A **85**, 163 (2006)
14. N.N. Nedyalkov, T. Sakai, T. Miyanishi, M. Obara, J. Phys. D Appl. Phys. **39**, 5037 (2006)
15. P. Leiderer, C. Bartels, J. Konig-Birk, M. Mosbacher, J. Boneberg, Appl. Phys. Lett. **85**, 5370 (2004)
16. M.F. Yanik, H. Cinar, H.N. Cinar, A.D. Chisholm, Y. Jin, A. Ben-Yakar, Nature **432**, 822 (2004)
17. U.K. Tirlapur, K. Konig, Nature **418**, 290 (2002)
18. N Shen, D. Datta, C.B. Schaffer, P. LeDuc, D.E. Ingber, E. Mazur, Tech Science Press **2**, 17 (2005)
19. A. Vogel, J. Noack, G. Huttman, G. Paltauf, Appl. Phys. B **81** 1015 (2005).
20. H. Hovel, S. Fritz, A. Hilger, U. Kreibig, M. Vollmer, Phys. Rev. B **48**, 178 (1993)
21. S. Nolte, B.N. Chichkov, H. Welling, Y. Shani, K. Lieberman, H. Terkel, Opt. Lett. **24**, 914 (1999)
22. H.C. van de Hulst, *Light Scattering by Small Particles*. Wiley, New York (1957)
23. U. Kreibig, M. Vollmer, *Optical Properties of Metal Clusters*. Springer, Berlin (1995)
24. M. Kerker, *The Scattering of Light and Other Electromagnetic Radiation*. Academic, New York (1969)
25. J.D. Jackson, *Classical Electrodynamic*. Wiley, New York, 3rd edition (1999)
26. C.F. Bohren, D.R. Huffman, *Absorption and Scattering of Light by Small Particles*. Wiley, New York (1983)

27. G.C. Papavassiliou, Prog. Solid State Chem. **12**, 185 (1979)
28. F.E. Wagner, S. Haslbeck, and L. Stievano L. et al. Nature, **407**, 691 (2000)
29. M. Kerker, J. Colloid Interface Sci. **105**, 297 (1985)
30. J. Yguerabide, E.E. Yguerabide, Analy. Biochem. **126**, 137 (1998)
31. M. Faraday, Philos. Trans. 147, 145 (1857)
32. G. Mie, Ann. Phys. 25, 377 (1908)
33. P. Debye, Ann. Phys. 30, 57 (1909)
34. R.L. Kelly, E. Coronado, L.L. Zhao, G.C. Schatz, J. Phys. Chem. B **107**, 668 (2003)
35. P. Drude, Ann. Phys. 1, 556 (1900)
36. P. Drude, Ann. Phys. 3, 369 (1900)
37. P. Drude, Ann. Phys. 7, 687 (1902)
38. H. Hovel, S. Fritz, A. Hilger, U. Kreibig, M. Vollmer, Phys. Rev. B **48**, 178 (1993)
39. D.D. Evanoff, G. Chumanov, J. Phys. Chem. B **108**, 13957 (2004)
40. U. Kreibig, L. Genzel, Surf. Sci. **156**, 678 (1985)
41. K.-P Charle, F. Frank, W. Schulze, Ber Bunsenges. Phys. Chem **88**, 350 (1984)
42. U. Kreibig, C.v. Fragstein, Z. Phys. **224**, 307 (1969)
43. U. Kreibig, J. Phys. F **4**, 999 (1974)
44. L. Genzel, T.P. Martin, U. Kreigbig, Z. Phys. B **21**, 339 (1975)
45. M.M. Alvarez, J.T. Khoury, T.G. Schaaff, M.N. Shafigullin, I. Vezmar, R.L. Whetten, J. Phys. Chem. B **101**, 3706 (1997)
46. S. Link, M.A. El-Sayed, J. Phys. Chem. B **103** 4212 (1999)
47. F. Bassani, G.P. Parravicini, *Electronic States and Optical Transitions in Solids*. Pergamon, New York (1975)
48. N.W. Ashcroft, N.D. Mermin, *Solid state Physics*. Saunders College, Philadelphia (1976)
49. R.H. Doremus, J. Chem. Phys. **40**, 2389 (1964)
50. R.H. Doremus, J. Chem. Phys. **42**, 414 (1965)
51. I. Euler, Z. Physik **137**, 318 (1954)
52. W.J. Doyle, Phys. Rev. **111**, 1067 (1958)
53. U. Kreibig, Z. Physik B **31**, 39 (1978)
54. A. Kawabara, R. Kubo, J. Phys. Soc. Japan **21**, 1765 (1966)
55. R. Ruppin, H. Yatom, Phys. Status Solidi (b) **74**, 647 (1976)
56. W.A. Kraus, G.C. Schatz, J. Chem. Phys. **79** 6130 (1983)
57. D.R. Penn, R.W. Rendell, Phys. Rev. B **26**, 3047 (1982)
58. M. Quinten, Z. Physik B **35**, 217 (1995)
59. B.J. Messinger, K. Ulrich von Raben, R.K. Chang, P.W. Barber, Phys. Rev. B **24**, 649 (1981)
60. M. Quinten, Appl. Phys. B **73**, 245 (2001)
61. J.M. Liu, Opt Lett. **7**, 196 (1982)
62. A. Ben-Yakar, R.L. Byer, J. of Appl. Phys. **98**, 5316 (2004)
63. S. Nolte, C. Momma, H. Jacobs, A. Tunnermann, B.N. Chichkov, B. Wellegehausen, H. Welling, J. Opt. Soc. Am. B **14,** 2716 (1997)
64. S.K. Sundaram, E. Mazur, Nat. Mat. **1,** 217 (2002)
65. J. Bonse, S. Baudach, J. Kruger, W. Kautek, M. Lenzer, Appl. Phys. A **74**, 19 (2002)

66. A. Plech, V. Kotaidis, M. Lorenc, J. Boneberg, Nat. Phys. **2**, 44 (2006)
67. B.S. Luk'yanchuk, Z.B. Wang, W.D. Song, M.H. Hong, Appl. Phys. A **79**, 747 (2004)
68. Y.W. Zheng, Dissertation, Nation university of Singapore (2002), pp. 57-59.
69. G.R. Jellison Jr., D.H. Lowndes, Appl. Phys. Lett., **51**, 352 (1987)
70. M. Lenzner, J. Kruger, S. Satania, Z. Cheng, C. Spielmann, G. Mourou, W. Kautek, F. Krausz, Phys. Rev. Lett. **80**, 4076 (1998).
71. J. Turkevich, P.C. Stevenson, J.A.Hiller, Discuss. Faraday Soc. **11** 55 (1951)
72. G. Frens, Nature Phys. Sci., **241**, 20 (1973)
73. L.V. Keldysh, Soviet Physics JETP **20**, 1307 (1965)
74. N. Bloembergen, IEEE J. Quant. Electron. **QE-10**, 375 (1974)
75. B.C. Stuart, M.D. Feit, S. Herman, A.M. Rubenchik, B.W. Shore, M.D. Perry, Phys. Rev. B **53**, 1749 (1996)
76. M. H. Niemz, Appl. Phys. Lett. **66**, 1181 (1995)
77. W. Kautek, J. Kruger, M. Lenzner, S. Sartania, C. Spielmann, F. Krausz, Appl. Phys. Lett. **69**, 3146 (1996)
78. P. Rudolph, J. Bonse, J. Kruger, W. Kautek, Appl. Phys. A: Mater. Sci. Process. **68**, S753 (1999)
79. H. Kuhn, in: W. Hoppe, W. Lohmann, H. Mark, H. Ziegler (Eds.) Biopkysik, Springer, Berlin, p. 289 (1982)
80. W. Rechberger, A. Hohenau, A. Leitner, F.R. Krenn, B. Lamprecht, F.R. Aussenegg, Opt. Comm. **220**, 137 (2003)
81. J. Sinzig, M. Quinten, Appl. Phys. A **58**, 157 (1994)
82. J. Sinzig, U. Radtke, M. Quinten, U. Kreibig, Z. Physik D **26**, 242 (1993)
83. X. Guo, A. Ben-Yakar, Nano Lett. (submitted)
84. J.P. Kottmann, O.J.F. Martin, D.R. Smith, and S. Schultz, Phys. Rev B **64**, 235402 (2001)
85. M. Specht, J.D. Pedarnig, W.M. Heckl, T.W. Haensch, Phys. Rev. Lett. **68**, 476 (1992)
86. G.T. Boyd, Th. Rasing, J.R.R. Leite, Y.R. Shen, Phys. Rev B **30**, 519 (1984)
87. J.T. Krug II, E.J. Sanchez, X.S. Xie, J. Chem. Phys. **116** 10895 (2002)
88. M.B. Mohamed, K.Z. Ismael, S. Link, M.A. El-Sayed, J. Phys. Chem B **102**, 9370 (1998)
89. S.S. Shankar, A. Rai, B. Ankamar, A. Singh, A. Ahmad, M. Sastry, Nature Mat. **3**, 482 (2004)
90. H. Wang, D.W. Brandl, F. Le, P. Nordlander, N.J. Halas, Nano Lett. **6**, 827 (2006)
91. D. Lapotko, E. Lukianova, M. Potapnev, O. Aleinikova, A. Oraevsky, Cancer Lett. **239**, 36 (2006)
92. B. Khlebtsov, V. Zharov, A. Melnikov, V. Tuchin, N. Khlebtsov, Nanotech. **17**, 5167 (2006)
93. K Sokolov, M. Follen, J. Aaron, I. Pavlova, A. Malpica, R. Lotan, R. Richards-Kortum, Cancer Res. **63**, 1999 (2003)
94. C. Sonnichsen, B.M. Reinhard, J. Liphardt, A.P. Alivisato, Nature Biotech. **23**, 741 (2005)

95. T. Kraus, L. Malaquin, H. Schmid, W. Riess, N.D. Spencer, H. Wolf, Nature Nanotech. **2**, 570 (2007)
96. M. Quinten, A. Leitner, J.R. Krenn, F.R. Aussenegg, Opt. Lett. **23**, 1331 (1998)
97. F. Burmeister et al, Languir **13**, 2983 (1997)
98. F. Burmeister et al, Appl. Surf. Sci. **144-145**, 461 (1999)

Vita

Daniel Steven Eversole was born in Winchester, Virginia, on July 27, 1982, the son of Ellen Francis Eversole and Kim Barton Eversole. After completing his work at Pennridge High School, Perkasie, Pennsylvania, in 2000, he entered the University of Rochester in Rochester, New York. He received the degrees of Bachelor of Science in the fields of Optics and Biomedical Engineering. His area of concentration was in Medical Optics. In addition to his bachelor's degree, he received a certificate in Ethnomusicology at the Eastman School of Music in Rochester, New York. In September 2004, he entered The Graduate School at The University of Texas at Austin.

Permanent Address: 108 W. 45th Street
Apt. 307
Austin, TX 78751

This thesis was typed by the author